

2
3 **How well do global ocean biogeochemistry models simulate dissolved iron**
4 **distributions?**

5
6 Alessandro Tagliabue¹, Olivier Aumont², Ros DeAth³, John P. Dunne⁴, Stephanie Dutkiewicz⁵,
7 Eric Galbraith⁶, Kazuhiro Misumi⁷, J. Keith Moore⁸, Andy Ridgwell^{3,9}, Elliot Sherman⁸, Charles
8 Stock⁴, Marcello Vichi^{10,11}, Christoph Völker¹² and Andrew Yool¹³

- 9
10 1. School of Environmental Sciences, University of Liverpool, Liverpool, UK
11 2. IRD-LOCEAN, Institut Pierre Simon LaPlace, 4 Place Jussieu, 75252 Paris Cedex 05, France.
12 3. School of Geographical Sciences, University of Bristol, Bristol, UK.
13 4. NOAA/Geophysical Fluid Dynamics Laboratory, 201 Forrestal Road, Princeton NJ 08540,
14 USA
15 5. Center for Global Change Science, Massachusetts Institute of Technology, Cambridge, MA
16 20139. USA.
17 6. ICREA-ICTA, Universitat Autònoma de Barcelona, Bellaterra, Barcelona, Spain
18 7. Environmental Science Research Laboratory, Central Research Institute of Electric Power
19 Industry, Abiko, Chiba, Japan.
20 8. Department of Earth System Science, University of California, Irvine, CA. USA.
21 9. Department of Earth Sciences, University of California, Riverside, CA 92521, USA
22 10. Department of Oceanography, University of Cape Town, Cape Town, South Africa
23 11. Nansen-Tutu Centre for Marine Environmental Research, Cape Town, South Africa
24 12. Alfred-Wegener-Institut, Helmholtz-Zentrum für Polar- und Meeresforschung,
25 Bremerhaven, Germany
26 13. National Oceanography Centre, University of Southampton Waterfront Campus, European
27 Way, Southampton, SO14 3ZH, UK

28
29 *Main Point 1:* First intercomparison of 13 global iron models highlights key challenges in
30 reproducing new iron data

31 *Main Point 2:* Wide uncertainty in iron input fluxes, which results in poorly constrained
32 residence times

33 *Main Point 3:* Reducing uncertainty in scavenging and biological cycling is a priority

34
35 **Abstract**

36
37 Numerical models of ocean biogeochemistry are relied upon to make projections about the
38 impact of climate change on marine resources and test hypotheses regarding the drivers of
39 past changes in climate and ecosystems. In large areas of the ocean, iron availability regulates
40 the functioning of marine ecosystems and hence the ocean carbon cycle. Accordingly, our
41 ability to quantify the drivers and impacts of fluctuations in ocean ecosystems and carbon
42 cycling in space and time relies on first achieving an appropriate representation of the
43 modern marine iron cycle in models. When the iron distributions from thirteen global ocean
44 biogeochemistry models are compared against the latest oceanic sections from the
45 GEOTRACES programme we find that all models struggle to reproduce many aspects of the
46 observed spatial patterns. Models that reflect the emerging evidence for multiple iron sources
47 or subtleties of its internal cycling perform much better in capturing observed features than
48 their simpler contemporaries, particularly in the ocean interior. We show that the substantial
49 uncertainty in the input fluxes of iron results in a very wide range of residence times across
50 models, which has implications for the response of ecosystems and global carbon cycling to
51 perturbations. Given this large uncertainty, iron-fertilisation experiments based on any single

52 current generation model should be interpreted with caution. Improvements to how such
53 models represent iron scavenging and also biological cycling are needed to raise confidence in
54 their projections of global biogeochemical change in the ocean.

55 56 **1. Introduction**

57
58 With the important role played by dissolved iron (DFe) in regulating ocean biogeochemical
59 cycles well established [Boyd and Ellwood, 2010], most three dimensional global
60 biogeochemistry models now include a prognostic DFe tracer as standard. These models
61 explicitly represent the DFe limitation of primary production that is prevalent across large
62 areas of the ocean [C M Moore et al., 2013]. This has allowed quantitative projections
63 regarding the impacts of environmental change in Fe-limited regions [Bopp et al., 2013], how
64 DFe may regulate glacial-interglacial changes to the global carbon cycle [Tagliabue et al.,
65 2009] and the wider role played by different nutrients as drivers of planktonic diversity
66 [Ward et al., 2013]. However, the robustness of these results is reliant on how a given model
67 represents the ocean DFe cycle. For example, a model that accounted for hydrothermal
68 sources of Fe was shown to be less sensitive to changes in aeolian iron supply than the same
69 model without a hydrothermal input [Tagliabue et al., 2010]. Equally, there is a six-fold
70 difference in the estimated impact of dust variations on glacial and interglacial changes in
71 atmospheric CO₂ (5-28 ppm) [Kohfeld and Ridgwell, 2009] that is largely driven by details of
72 the modeled DFe cycle.

73
74 In brief, the ocean iron cycle is regulated by a complex array of different processes [Boyd and
75 Ellwood, 2010]. DFe is thought to be supplied to the ocean from atmospheric deposition
76 [Jickells et al., 2005], continental margins [Elrod et al., 2004] and hydrothermal vents
77 [Tagliabue et al., 2010], with potential emerging roles for input from rivers [Rijkenberg et al.,
78 2014], icebergs [Raiswell et al., 2008] and glaciers [Gerringa et al., 2012]. DFe is relatively
79 insoluble in oxygenated seawater and DFe levels are maintained to a large part due to
80 complexation with organic ligands that bind Fe [Gledhill and Buck, 2012]. Unbound, or free Fe
81 can then precipitate as solid forms or be scavenged by particles [Bruland et al., 2014]. DFe is
82 operationally defined by the filter size (usually 0.2µm) and over half of the DFe pool can be
83 colloidal [Boye et al., 2010; Fitzsimmons and Boyle, 2014; Wu et al., 2001]. This implies that the
84 aggregation and coagulation of colloidal Fe, termed 'colloidal pumping' [Honeyman and
85 Santschi, 1989], may also be an important loss of DFe. As a divalent metal, Fe also undergoes
86 rapid redox transformations between Fe(II) and Fe(III) species mediated by oxidation,
87 reduction and photochemical processes [Wells et al., 1995]. The biological cycling of Fe is also
88 complex with varying cellular requirements for Fe [Raven, 1988; Raven et al., 1999] and the
89 role of luxury uptake [Marchetti et al., 2009] driving a wide range in phytoplankton Fe quotas
90 [Sunda and Huntsman, 1997; Twining and Baines, 2013]. Equally, the recycling of DFe by
91 bacteria, viruses and zooplankton is emerging as a key component in governing the Fe supply
92 to phytoplankton [Barbeau et al., 1996; Boyd et al., 2012; Hutchins and Bruland, 1994;
93 Strzepek et al., 2005]. Lastly, process studies and basin scale data syntheses have highlighted
94 important specificities to the remineralisation lengths scale and vertical profile of DFe,
95 relative to other nutrients [Frew et al., 2006; Tagliabue et al., 2014c; Twining et al., 2014].

96
97 The earliest global iron models were informed by the first efforts to synthesise the emerging
98 datasets on DFe in the late 1990s [Johnson et al., 1997]. These models only considered a dust
99 source, applied constant phytoplankton Fe demands and inferred that the seemingly constant
100 deep ocean DFe concentrations indicated a threshold stabilisation of DFe by organic ligands
101 [Archer and Johnson, 2000; Lefèvre and Watson, 1999]. As available DFe datasets expanded, it
102 became clear that deep ocean concentrations were more regionally and temporally varied

103 than accounted for by these models and that explicitly computing un-complexed DFe led to a
104 better model-data agreement [Parekh et al., 2004]. At the same time, assumptions regarding
105 fixed iron solubility in dust and constant C:Fe ratios in exported organic matter were being
106 questioned and alternatives tested [Ridgwell, 2001; Watson et al., 2000]. Towards the end of
107 the Joint Global Ocean Flux Study (JGOFS) era more complicated treatments of the demand for
108 DFe from different phytoplankton groups also emerged and when coupled to realistic models
109 of ocean circulation, provided the first estimates of the areal extent of DFe limitation [Aumont
110 et al., 2003; Moore et al., 2002]. In more recent years, and particularly with the advent of the
111 GEOTRACES programme (www.geotraces.org), observations of DFe have expanded rapidly
112 [Mawji et al., 2015; Tagliabue et al., 2012]. This has driven the representation of DFe sources
113 associated with margin sediments [Moore and Braucher, 2008] and hydrothermal vents
114 [Tagliabue et al., 2010] in models. At the same time efforts to account for redox speciation
115 [Tagliabue and Völker, 2011] and variability in Fe binding ligands [Misumi et al., 2013; Völker
116 and Tagliabue, 2015] in global models have also been undertaken.

117
118 Until now there has been no comprehensive effort to evaluate how different global models
119 represent DFe, apart from the one off model-data comparisons typical of individual
120 publications [Moore and Braucher, 2008; Tagliabue et al., 2008]. Our maturing vision of the
121 oceanic distribution of DFe and our deeper understanding of how it interacts with broader
122 biogeochemical cycles now allows a more widespread intercomparison of global iron models.
123 In conducting the first ‘iron model intercomparison project’ (FeMIP) we aim to intercompare
124 as broad a suite as possible of global ocean biogeochemistry models with a focus on the
125 reproduction of features present in the full depth ocean sections emerging from the
126 GEOTRACES programme. In doing so we highlight the challenges present for global ocean
127 biogeochemistry models in simulating the distribution of DFe, which emerges as unique to
128 that of other nutrients.

129 130 **2. Methodology**

131 132 **2.1 Intercomparison process**

133
134 The goal of this study was to include as many global iron models as possible in order to
135 ensure a ‘state of the art’ view on their representation of Fe cycling. In that regard, our
136 thirteen models (Table 1) range from those used in the recent IPCC report for coupled
137 climate-carbon studies, to those focused on global patterns of Fe cycling and effects on ocean
138 biogeochemical cycles and phytoplankton diversity, to those concerned with geological
139 timescales. This inclusive design thus did not impose a rigid set of guidelines regarding the
140 model forcings, as done for the ocean carbon-cycle model intercomparison (OCMIP) and
141 climate model intercomparison (CMIP) projects. While imposing identical ocean circulation
142 or external forcing scenarios would have permitted a more direct cross comparison of the
143 different iron models, the extra constraints would have drastically reduced the number of Fe
144 models able to participate and hinder our aim to account for the full diversity of Fe models.
145 Groups submitted their best representation of the dissolved iron distribution in netCDF
146 format at monthly frequency for a canonical year on their standard model grid, alongside
147 additional requested information (temperature, salinity, nitrate, phosphate and silicic acid
148 concentrations, where available). We compiled model data from thirteen model
149 configurations: BEC [J K Moore et al., 2013], BFM [Vichi et al., 2007], BLINGv0 [Galbraith et al.,
150 2010], COBALT [Stock et al., 2014], GENIE (Fe scheme as summarised by [Matsumoto et al.,
151 2013]), MEDUSA1 [Yool et al., 2011], MEDUSA2 [Yool et al., 2013], MITecco [Dutkiewicz et al.,
152 2015], MITigsm [Dutkiewicz et al., 2014], PISCES1 [Aumont et al., 2015], PISCES2 [Resing et al.,
153 2015; Völker and Tagliabue, 2015], REcoM [Hauck et al., 2013] and TOPAZ [Dunne et al.,

154 2013], all implemented at the global scale. All models were then regridded onto a $1^\circ \times 1^\circ$
155 horizontal grid with 33 vertical levels (bounded by 0, 10, 20, 30, 40, 50, 75, 100, 125, 150,
156 200, 250, 300, 400, 500, 600, 700, 800, 900, 1000, 1100, 1200, 1300, 1400, 1500, 1750, 2000,
157 2500, 3000, 3500, 4000, 4500, 5000 and 5500m) as a common FeMIP grid.

158

159 **2.2 Observational datasets**

160

161 Observations of dissolved iron are taken from two sources. Firstly, we use an updated version
162 of a global DFe database [Tagliabue *et al.*, 2012] with approximately 20,000 individual
163 observations. This database was gridded at monthly resolution on the FeMIP grid to compare
164 models and observations grid cell by grid cell and month by month, with no volume
165 weighting. Secondly, we extracted DFe data from recent GEOTRACES sections from the 2014
166 intermediate data product [Mawji *et al.*, 2015]. For comparison purposes (Sec 3.2) the
167 modeled DFe from the longitude, latitude and month of each sampling station was then
168 extracted and the observed data was regridded on the same 33 vertical levels as the models
169 (averaging where more than one observation was present in a particular depth bin). We use
170 datasets collected on the GA-02 West Atlantic cruise [Rijkenberg *et al.*, 2014], the GA-03 North
171 Atlantic zonal transect [Hatta *et al.*, 2014], the CoFeMUG south Atlantic zonal cruise [Saito *et*
172 *al.*, 2013], the GIPY-6 Atlantic sector of the Southern Ocean cruise [Chever *et al.*, 2010; Klunder
173 *et al.*, 2011] and the recently completed GP-16 Equatorial Pacific zonal section [Resing *et al.*,
174 2015] that is not yet in the GEOTRACES data product. We note that all IDP2014 GEOTRACES
175 data [Mawji *et al.*, 2015] is also included in the global dataset.

176

177 **2.3 Brief introduction of the different iron models**

178

179 The goal here is not to exhaustively describe the FeMIP models for which we refer to the
180 original publications. Rather we seek to summarise how the models treat key components of
181 the Fe cycle and to highlight important differences (Table 1). In our summary we focused on
182 how each model treated the sources of Fe, the chemistry of Fe (including the representation of
183 Fe binding ligands, how free Fe is computed and whether scavenging is a first order rate or a
184 second order function of particle concentrations), biological cycling of Fe (if Fe/C ratios were
185 variable and if zooplankton excretion of Fe depends on the Fe content of prey) and particle Fe
186 dynamics (how many particle pools were simulated and whether the Fe regeneration
187 efficiency was unique or coupled to organic matter).

188

189 All models considered a dust source of Fe and only BFM, GENIE and MEDUSA1 did not
190 consider sedimentary Fe supply, only BEC, BFM, PISCES1 and PISCES1 include river input of
191 Fe, while BEC and PISCES1 and PISCES2 are the only models that represent hydrothermal Fe
192 input. All models except BEC compute the free Fe concentration that can be scavenged based
193 on Parekh *et al.* [2004] and all except BFM, COBALT, MEDUSA1 and MEDUSA2 have a second
194 order scavenging rate, i.e. a dependency on particle concentrations. Only PISCES1 and
195 PISCES2 include a representation of colloidal losses of dFe, based on aggregation of dissolved
196 organic material [Aumont *et al.*, 2015]. It is notable that despite a maturing understanding of
197 the variations in the concentrations of Fe binding ligands [Gledhill and Buck, 2012], most
198 FeMIP models still assume a constant ligand concentration (as per the earliest Fe models) that
199 is 1 nM for all models except BFM and PISCES1 who use 0.6 nM. Two exceptions in this regard
200 are PISCES2 and TOPAZ. TOPAZ applies an empirical relationship to dissolved organic carbon
201 (DOC) to derive ligand concentrations (5×10^{-5} mol ligand per mol DOC). PISCES2 is the only
202 FeMIP model to represent a dynamic ligand pool with explicit sources and sinks [Völker and
203 Tagliabue, 2015] and a variable computation of the colloidal Fe fraction [Liu and Millero,
204 1999], modified to account for hydrothermal ligand supply [Resing *et al.*, 2015]. BLING

205 switches off Fe scavenging when oxygen drops below 1 mmol m⁻³ [Galbraith *et al.*, 2010] and
206 both BLING and COBALT reduce the stability of Fe-ligand complexes in the presence of light
207 [Galbraith *et al.*, 2010; Stock *et al.*, 2014]. Both the MITecco and MITigsm models cap DFe to a
208 maximum value of 1.3 nM with any excess Fe being numerically deleted. Due to the noted
209 flexibility in planktonic demands for Fe [Sunda and Huntsman, 1997; Twining and Baines,
210 2013], almost all FeMIP models have variable Fe/C ratios, with only MEDUSA1, MEDUSA2,
211 MITecco and MITigsm retaining fixed Fe/C ratios. Recycling by zooplankton is variable in
212 some FeMIP models and thus dependent on an assumed zooplankton Fe quota, except for
213 BEC, BLING, MEDUSA1, MEDUSA2 and REcoM where there is a fixed rate of recycling. Lastly,
214 all models include one particulate Fe pool, except PISCES1 and PISCES2 that consider 2 and
215 BEC, which represents sinking implicitly (accounting for ballasting). Only COBALT invokes
216 reduced regeneration efficiency relative to organic material that elongates the regeneration
217 depth-scale beyond that that for sinking organic material [Stock *et al.*, 2014].
218

219 Finally, it is notable several models were only run for a few decades or centuries (BEC, BFM,
220 COBALT, MEDUSA1, MEDUSA2, MITecco and MITigsm), a time comparable to the respective
221 residence time of Fe in the model in some cases, making them potentially more sensitive to
222 their initial conditions. This issue is discussed in more detail in Sec. 3.1.1.
223

224 **3. Results**

225 **3.1 Inter-model differences in dissolved iron distributions and cycling**

226 **3.1.1 Iron fluxes and residence times**

227
228 Beginning with an integrated view, there is substantial variability in the modeled Fe residence
229 times across the FeMIP models with two broad groupings of a few years and a few hundred
230 years (Table 2). Across the thirteen models, all include dust sources, ten include sediment
231 sources, but only three include hydrothermal and riverine Fe sources, respectively (Table 2).
232 Even for a given source, there is substantial inter-model difference in its strength. For
233 example, dust fluxes of dissolved iron range from ~1 to >30 Gmol Fe yr⁻¹ between models
234 (Table 2, accounting for any inter-model variations in solubility and mineral fraction). These
235 inter-model differences across all input fluxes result in a wide range of total iron inputs to the
236 ocean (66.9±67.1 Gmol Fe yr⁻¹, Table 1). In contrast we find a surprising degree of agreement
237 in the mean ocean iron concentration (0.58±0.14 nM, Table 2) from the models, with slightly
238 greater inter-model differences in the total integrated inventory of Fe reflecting different
239 model grid sizes (e.g. some models do not include the Arctic Ocean or the Mediterranean).
240 Ultimately this results in a wide range of residence times of dissolved iron in the models (~5
241 to > 500 years, Table 2) that reflects different assumptions regarding the strength of the
242 sources of DFe to the ocean, compensated by variable scavenging rates in order to reproduce
243 the observed DFe concentration.
244
245

246
247 The derivation of the residence time for Fe from each model allows us to evaluate the impact
248 of the shorter runs performed for some models. Taken at face value, even the relatively short
249 runs performed by almost all the models (except BFM, MEDUSA1 and perhaps also MEDUSA2)
250 are more than twice the residence time for Fe in that particular model. Nevertheless, it should
251 be noted that many of these residence times for the global ocean are likely skewed towards
252 lower values due to strong local sources that have a muted wider influence. For example,
253 much of the interior Fe distribution in the PISCES1 model has been shown to be linked to a
254 subducted preformed component [Tagliabue *et al.*, 2014b], suggesting that the deep ocean
255 equilibration timescale in this model, at least, must be much longer than the 11 years of its

256 average residence time. This is likely to be the case for models that employ a formulation for
257 the rate of DFe scavenging that depends on particulate fluxes, as biogenic fluxes in the ocean
258 interior are considerably slower than near the surface where sedimentary and dust sources
259 are dominant. Feedbacks will also exist between DFe inventory and biological fluxes, meaning
260 that a ~1000 yr time-scale component to the overall equilibrium adjustment will exist that
261 involves the redistribution of major nutrients globally. As such, this raises questions
262 regarding the distributions of Fe in the ocean interior for models that are only run for a few
263 decades, even if that is longer than the average residence time.

264

265 **3.1.2 Statistical assessment of FeMIP models**

266

267 In order to provide a general picture of variability amongst the models, we examine
268 correlations between observed and simulated DFe at the same locations (Table 3). When
269 viewed globally throughout the entire water column, correlations between observations and
270 the models can be as high as 0.51, while some are even anti-correlated. The mean biases
271 against observations are between -0.02 and -0.48 nM. In the 0-100m depth stratum, where Fe
272 is likely to be playing a role in regulating phytoplankton growth rates, all but one of the model
273 correlations fall between 0.33 and 0.48, implying no clear link between model complexity and
274 strength of correlation. On the other hand, the mean biases range from -0.29 to 0.67 nM,
275 which suggests less overall agreement in the absolute DFe levels. The 100-500 m depth
276 slice has the overall highest correlations, and all but three models reach their highest
277 correlations in this depth range. In the abyssal layers only the three models that consider
278 hydrothermal iron input (BEC, PISCES1 and PISCES2) show a reasonable correlation with
279 observations ($R=0.20$ to 0.35 , other models are < 0.15), highlighting the importance of this
280 source in the deep ocean. However, the inclusion of hydrothermal iron input does not
281 obviously lead to a significant improvement in the surface ocean. Similarly, including (or not)
282 sedimentary Fe input does not seem closely linked to reproducing observations in the surface
283 or intermediate layers. For example the two versions of MEDUSA with and without
284 sedimentary iron input do not show much difference in their correlation coefficients. It is also
285 important to note that we lack substantial coastal DFe datasets where sediments and/or river
286 supply results in high DFe levels in a number of models (see Sec 3.1.3). Section 3.2 will more
287 closely examine the different models using recent large-scale GEOTRACES sections as case
288 studies in different ocean regions.

289

290 **3.1.3 Inter-model differences in dissolved iron**

291

292 To examine the inter-model differences in dissolved iron in more detail, we compare the
293 model mean DFe over the 0-100m, 100-500m, 500-1000m and 2000-5000m depth slices,
294 repeating the analysis for the boreal (30-90N), tropical (30N-30S) and austral latitudes (90S-
295 30S). This enables us to group the models into 'high', 'moderate' and 'low' in terms of their
296 DFe distribution, relative to the full model suite (Figure 1). Comparing Figure 1 with the
297 statistical summary (Table 3) suggests that the inter-model trend in the average DFe
298 concentration for the different depth slices does not always reflect good statistical agreement
299 with the observations. However, it should be noted that while the inter-model trends in
300 average DFe reflect full spatial and temporal averages, the statistics determined from
301 observations only concern locations with available DFe observations (which is not spatially
302 and temporally complete).

303

304 Beginning with the surface ocean (0-100m) that is heavily influenced by surface sources and
305 biological uptake. MEDUSA1, MEDUSA2 and TOPAZ are consistently relatively high in iron for
306 all three latitudinal zones, including the Fe limited Southern latitudes. BEC is also relatively

307 rich in Fe, but only in the northern and tropical latitudes. The lowest DFe concentrations in all
308 three geographic zones are simulated by the BLING, COBALT and MITigsm models, with the
309 remaining models intermediate throughout.

310
311 The relative tendencies between the different FeMIP models are generally conserved in the
312 100-500m and 500-1000m depth slices that are more heavily influenced by remineralisation
313 processes. Notable departures from this general trend are PISCES2 displaying relatively
314 higher DFe levels in both depth bins. While both BFM and REcoM become more DFe rich in
315 the 500-1000m depth bin, TOPAZ stands out less as a high DFe model. In terms of
316 hemispheric contrasts, BEC becomes lower in DFe in the Southern region; otherwise the inter-
317 model trends are preserved.

318
319 In the deepest depth bin deep ocean sources such as hydrothermal vents, as well as sediments
320 are important. Unsurprisingly, the models that include hydrothermal vent DFe sources (BEC,
321 PISCES1 and PISCES2) show high DFe levels. In contrast, the high DFe levels for BFM,
322 MITecco, MITigsm and REcoM cannot be ascribed to hydrothermal DFe input and may be
323 related to initial conditions (e.g. for BFM) or deep ocean transport of high DFe levels.
324 However, it is notable that BFM, MITecco, MITigsm and REcoM do not perform well
325 statistically in this depth range (Table 3). The BLING and MEDUSA1 models simulate the
326 lowest concentrations in this depth bin. For a large number of models (BLING, GENIE,
327 MEDUSA1, MEDUSA2, TOPAZ), DFe concentrations decline in the 2000-5000m bin, relative to
328 the 500-1000m bin.

329

330 **3.1.4 Surface DFe distributions in the models**

331

332 Due to its role as a limiting nutrient, we explore the simulated annual mean surface DFe
333 concentrations from the FeMIP models in more detail (Figure 2, upper 50m average). Here we
334 see that, as suggested by the range in the model biases (Table 3), there is a substantial degree
335 of inter-model discord in the surface Fe distributions. Most models agree that the highest DFe
336 concentrations are found underneath the Saharan dust plume in the tropical Atlantic, but
337 others also emphasise dust supply into the Arabian Sea and enhanced DFe along the
338 continental margins. A large number of the models suggest the lowest DFe concentrations are
339 found across the Pacific Ocean. Exceptions are GENIE and MEDUSA1, who have much higher
340 DFe concentrations therein and BEC, MEDUSA2 and TOPAZ, who restrict low DFe to the south
341 Pacific only. The sub-Arctic Pacific is much more DFe deplete in BFM, MITecco and MITigsm
342 relative to the other FeMIP models. When the seasonality in DFe (presented as the maximum
343 minus minimum DFe concentration over the year, Figure 3) is compared, strong inter-model
344 differences also emerge. For example, some models show remarkably little seasonality (BFM,
345 GENIE, MEDUSA1, MEDUSA2 and MITigsm), whereas others have large seasonal cycles over
346 wide areas (>0.5nM, BEC, MITecco, PISCES1, PISCES2 and TOPAZ). This illustrates where high
347 annual mean concentrations in these regions are masking strong seasonal minima. For this
348 reason it is not straightforward to compare the models against observed Fe that might have
349 been collected during different seasons. At this stage, incomplete sampling over the seasonal
350 cycle is prevalent for virtually all locations with DFe measurements [Tagliabue *et al.*, 2012],
351 which precludes the mapping of DFe seasonality from observations. Table 3 is therefore more
352 suited for a statistical assessment of the surface DFe for a given model against all available
353 observations (where seasonal variations are accounted for by comparing model and data DFe
354 at identical longitudes, latitudes, depths and months).

355

356 **3.2 Comparison to recent GEOTRACES ocean sections**

357

358 To more closely examine how the different DFe models represent the observed distribution of
359 DFe we focus on a range of recent GEOTRACES sections. As described above (Sec 2.2) each
360 model is extracted at the exact location of the sampling locations, with the observations
361 regridded onto the same vertical grid. We refer the readers to the below cited papers for a
362 more complete discussion of each observational section and additional interpretation. In this
363 assessment we emphasise the key features observed on each section and how different
364 models are able to reproduce them. Because of this goal and because a given model may do a
365 good job of reproducing one feature, but not another, we did not perform statistical
366 assessments of the individual models for each section.

367

368 **3.2.1 West Atlantic**

369

370 The GA-02 West Atlantic meridional section provides unprecedented coverage of DFe
371 concentrations along the Atlantic Ocean, as well as insights into different mechanisms that
372 control the cycling, regeneration and supply of DFe [Rijkenberg *et al.*, 2014]. The key features
373 of this section are (i) low surface DFe in both the northern and southern end member surface
374 waters, (ii) a surface DFe enrichment around 20°N in the tropics and associated with a
375 subsurface DFe minima, (iii) a strong DFe regeneration maxima at 5-10°N centered around
376 500-1000m, (iv) a hydrothermal signal at around 5°S and between 2000-3000m depth and
377 (v) a hotspot of DFe that is present over much of the water column associated with the
378 confluence of the Brazil and Falklands current at around 35-40°S.

379

380 *Model representation of key features* (Figure 4): (i) Almost all models capture low DFe in the
381 Southern end member surface waters, except MEDUSA1 and MEDUSA2 and perhaps also
382 REcoM and TOPAZ. However it is only in BFM and COBALT, and to a lesser degree BEC, BLING,
383 MITigsm, PISCES1 and PISCES2 that reproduce the observed low DFE concentrations
384 associated with the northern endmember surface waters. (ii) A surface DFe enrichment
385 (presumably from dust) around 20°N is clearly present in BEC, MEDUSA1, MEDUSA2,
386 MITecco, MITigsm, PISCES1, PISCES2, REcoM and TOPAZ, but is less apparent in other models
387 (BFM, BLING, COBALT, GENIE). Nevertheless, in MEDUSA2, REcoM and TOPAZ the influence
388 of surface dust deposition appears to be much greater than is observed. Only PISCES1,
389 PISCES2 and COBALT, show the observed subsurface minima in DFe below the dust signal.
390 (iii) With respect to the strong DFe regeneration maxima at 5-10°N centered around 500-
391 1000m, COBALT displays a regeneration maximum at around the right depth level, while in
392 BEC high concentrations appear to be smeared from surface to the sea floor. In all other
393 models the regeneration signal in DFe is generally too small or absent and where it is present
394 (e.g. BFM, BLING, GENIE) it is generally too shallow in the water column. (iv) Concerning the
395 hydrothermal signal at around 5°S and between 2000-3000m depth, of the three models that
396 include hydrothermal DFe input, only PISCES2, with a greater longevity of hydrothermal Fe
397 [Resing *et al.*, 2015], shows a hint of DFe enrichment in the right location. MEDUSA2
398 underestimates DFe in the ocean interior along the entire Atlantic section. (v) No models
399 capture the elevated DFe over almost the entire water column around 35-40°S. In the
400 observations, this is ascribed to the offshore export of Brazilian shelf waters or DFe input
401 from the dissolution of particulate Fe associated with the Rio de la Plata river [Rijkenberg *et*
402 *al.*, 2014].

403

404 **3.2.2 Subtropical North Atlantic**

405

406 The GA-03 North Atlantic zonal section crossed the subtropical North Atlantic between Cape
407 Verde and Woods Hole (USA) via Bermuda. Key signals in the dataset [Hatta *et al.*, 2014] are
408 (i) strong enhancements in DFe associated with DFe regeneration and also coastal input along

409 the eastern and western margins, (ii) a surface enrichment along with a subsurface minimum
410 in DFe and (iii) a strong hydrothermal anomaly over the mid Atlantic ridge.

411

412 *Model representation of key features* (Figure 5): (i) Enhanced DFe in the subsurface along the
413 margins is represented to different degrees by the FeMIP models. BLING, COBALT, MITecco
414 and PISCES1 have hints of subsurface maxima in DFe along the eastern margin. It is
415 encouraging that the addition of ligand production during remineralisation in PISCES2 clearly
416 improves the intensity of the remineralised DFe signal. However, none of these models have a
417 broad homogenous signal (down to > 2000m) of elevated DFe that is observed on the eastern
418 margin, except perhaps BEC, which has a strong subsurface maximum that spreads over all
419 depth levels. (ii) The subsurface minima in DFe underlying a surface (presumably dust)
420 enrichment is captured clearly by COBALT, PISCES1 and PISCES2 and slightly less clearly by
421 BEC, BFM and BLING. (iii) A hydrothermal anomaly is present in PISCES1, but closer in
422 magnitude to the observations in PISCES2, while BEC also displays a strong hydrothermal
423 signal. COBALT displays a sediment signal at depth that is not reproduced by the
424 observations. It also notable that many of the models present an 'inverted' DFe profile, with
425 decreasing DFe concentrations towards the ocean interior (GENIE, MEDUSA1, MEDUSA2,
426 REcoM and TOPAZ), which could be indicative of too great a residence time for DFe at the
427 ocean surface. Also, BLING, COBALT, MEDUSA2 and TOPAZ seem to be systematically too low
428 in terms of their interior ocean DFe levels across this section.

429

430 **3.2.3 Subtropical South Atlantic**

431

432 The CoFeMUG section traversed the south Atlantic between Namibia and Brazil and had the
433 following notable signatures [*Noble et al., 2012; Saito et al., 2013*]: (i) a remineralisation
434 signal and/or sediment input on the eastern margin, (ii) low overall surface concentrations
435 and (iii) a strong hydrothermal signal at depth.

436

437 *Model representation of key features* (Figure 6): (i) Interestingly, more models are able to
438 simulate a remineralisation signal on the eastern side of the basin (COBALT, MEDUSA1,
439 MEDUSA2, MITecco, PISCES1, PISCES2, REcoM and TOPAZ) for this section than for the GA03
440 section. Although for some models this feature is too weak or spread over too many depth
441 levels. (ii) All models, except MEDUSA1, MEDUSA2, REcoM and TOPAZ, are able to reproduce
442 the overall low DFe conditions in the surface waters. (iii) BEC and PISCES1 represent a DFe
443 anomaly over the ridge as observed, but this is underestimated. PISCES2 represents a
444 stronger hydrothermal signal, but it appears to spread too far off-axis relative to that
445 observed. Again, COBALT displays a strong sediment signal in the deep ocean that is not
446 observed. BFM, BLING, MEDUSA2 and to some extent TOPAZ underestimate interior ocean
447 DFe levels.

448

449 **3.2.4 Southern Tropical Pacific**

450

451 The GP-16 cruise ran from Ecuador to Tahiti [*Resing et al., 2015*] and displays the following
452 key features: (i) DFe enrichment along the eastern margin over almost the entire water
453 column, (ii) low surface concentrations and (iii) a remarkable hydrothermal plume
454 propagating westward for > 4000km from the East Pacific Rise to at least 150°W.

455

456 *Model representation of key features:* (Figure 7), (i) BEC, COBALT, PISCES2 and TOPAZ are the
457 only models able to produce the broad signal of elevated DFe throughout the entire water
458 column on the eastern margin. BLING, MEDUSA1, MEDUSA2 and REcoM display an
459 enrichment in DFe but this remains more tightly localised than observed. (ii) All models

460 capture the low DFe levels typical of Pacific surface waters, but for some models (BFM, BLING,
461 COBALT, GENIE, MEDUSA2 and TOPAZ), low DFe is also too prevalent in the ocean interior.
462 (iii) BEC and PISCES1 capture a local hydrothermal signal above the East Pacific Rise, but only
463 PISCES2 goes any way towards reproducing the degree of off axis transport. As seen
464 previously, MITigsm and COBALT show DFe increases near the sea floor, but these are more
465 widespread than seen in the observations. As noted previously, BFM, BLING COBALT,
466 MEDUSA2 and TOPAZ show too little DFe in the ocean interior ($<0.3\text{nM}$), relative to the
467 observations ($>0.6\text{ nM}$ away from the hydrothermal plume).

468

469 **3.2.5 Southern Ocean – Atlantic Sector**

470

471 Both the GIPY-4 and GIPY-5 cruises ran from Cape Town (South Africa) to the Antarctic
472 continent along the so-called ‘GoodHope’ line during the International Polar Year [*Chever et*
473 *al.*, 2010; *Klunder et al.*, 2011]. These cruises sampled at different resolutions north and south
474 of the Polar Front and have been blended to form one section. Notable features in this dataset
475 include (i) low but non zero concentrations at the surface that propagate into the subsurface,
476 (ii) a strong remineralisation signal at around 500m near 60S and (iii) a strongly local
477 hydrothermal signal over the Bouvet region ridge crest at around 54°S and more widespread
478 elevated DFe in the abyssal ocean north of the ridge (i.e. between $\sim 54^\circ\text{S}$ and the northern end
479 of the transect).

480

481 *Model representation of key features:* (Figure 8), (i) Most models display low overall DFe
482 concentrations at the surface. GENIE, MEDUSA1, MEDUSA2 and to a lesser degree REcoM and
483 TOPAZ over estimate surface DFe concentrations. But even the models that have low surface
484 DFe show rapid increases with depth, indicating that the ferricline is too shallow in all models.
485 (ii) No FeMIP model captures the remineralisation signal seen in the subsurface just south of
486 the Polar Front. (iii) Despite including a hydrothermal source, BEC is unable to represent the
487 local hydrothermal enrichment. While PISCES1 represents a slight hydrothermal anomaly
488 that appears to be from an adjacent source, the longer lifetime of hydrothermal Fe in PISCES2
489 leads to the anomaly being too widespread in the abyssal ocean. On the other hand, both BEC
490 and PISCES2 do show elevated DFe in the abyssal ocean north of the main ridge at 54°S that
491 compares well with the data. COBALT, MITecco and MITigsm again show a sediment signal in
492 DFe at depth, while COBALT and TOPAZ show very high values near the Antarctic coast. None
493 of these features are observed in the dataset. The BFM stands out from the other models with
494 the large underestimation of DFe in the Southern Ocean interior as already seen for the GA-02
495 section.

496

497 **4. Discussion**

498

499 **4.1 Examining inter-model differences in Fe distributions relative to other nutrients**

500

501 In short, we find a wide range of simulated DFe distributions from current global ocean
502 biogeochemical models that reflects an apparent lack of inter-model agreement in the
503 processes that control the oceanic distribution of DFe. When assessed against the best DFe
504 datasets, most models perform modestly both quantitatively in terms of magnitudes and
505 patterns, and qualitatively in representing the inferred mechanisms. This has important
506 implications for how models are used to understand biogeochemical cycles [*Galbraith et al.*,
507 2010; *Moore et al.*, 2002; *Tagliabue et al.*, 2014a], planktonic diversity and resource
508 competition [*Dutkiewicz et al.*, 2012; *Ward et al.*, 2013], as well as the ocean response to
509 fluctuations in the environment in general [*Bopp et al.*, 2013; *Dutkiewicz et al.*, 2013;
510 *Tagliabue et al.*, 2009]. It is noteworthy that this inter-model disagreement appears to be

511 solely driven by the particular way in which different models represent the Fe cycle. If we
512 examine the models in terms of macronutrients (nitrate and phosphate) then, taking the long
513 meridional GA02 section as example, we see a much stronger inter-model and model-data
514 agreement (Figures 9 and 10). Although inter-model differences due to specific physical
515 models are visible in the Atlantic water mass structure, the mechanisms driving the N and P
516 cycles are similar.

517

518 We further contextualise the inter-model Fe differences by examining how they represent the
519 relative inventories of Fe and NO_3 in the ocean interior by plotting the Fe^* tracer ($\text{Fe} -$
520 $\text{NO}_3 \cdot r_{\text{Fe}/\text{N}}$). Defining $r_{\text{Fe}/\text{N}}$ in the same way as for the GA02 section [Rijkenberg *et al.*, 2014]
521 (based on the observed Fe:apparent oxygen utilisation relationship, which results in a Fe/N
522 ratio of 0.47 mmol/mol) and using PO_4 (and a NO_3/PO_4 ratio of 16/1) for GENIE and BLING,
523 which do not simulate NO_3 , allows us to examine DFe concentrations relative to NO_3 , (Figure
524 11). The data shows relatively replete waters originating from the northern hemisphere
525 linked to North Atlantic Deep Water (NADW), which becomes flanked above and below by
526 relatively Fe poor water from the southern hemisphere linked to Antarctic Intermediate
527 Water (AAIW) and Antarctic Bottom Water (AABW). There is also a zone of relatively
528 depleted Fe in the subsurface overlying the NADW signal in the northern hemisphere likely
529 linked to northern subtropical mode water. In these sections we can see that NADW is
530 relatively impoverished in DFe in MEDUSA1, MEDUSA2 and TOPAZ, despite these models
531 generally overestimating surface DFe. This may indicate an overly short lifetime for Fe away
532 from the surface and subsequent lack of permanence in the NADW signal. Looking at
533 southern sourced waters, all models except BFM perform well (notwithstanding the northern
534 sourced water biases). Obviously, this comparison should only be taken as indicative since
535 different models are underpinned by different relationships between NO_3 and Fe and the
536 actual planktonic Fe:N ratio can vary from the value chosen in the Rijkenberg *et al.* [2014]
537 study [Twining and Baines, 2013]. Nevertheless, it does provide an additional means to assess
538 the relative transport of Fe and NO_3 through the ocean interior.

539

540 **4.2 Identifying the key processes at different depth strata**

541

542 One important inter-model difference that clearly impacts the agreement with observations
543 and the role of Fe on biota is the strong surface enrichments evident in some models
544 (MEDUSA1, MEDUSA2, REcoM and TOPAZ). In the observations, any Fe enrichments due to
545 dust deposition are far more localised and apparently short lived in space (e.g. Figures 4 and
546 5). For the models surface overestimation of iron implies either too large an iron source or
547 that the residence time for Fe at the surface is too long. The latter possibility highlights the
548 importance of how models treat the scavenging process and could also be linked to constant
549 Fe/C ratios that do not permit 'luxury uptake' of Fe at high DFe concentrations (specifically
550 MEDUSA1, MEDUSA2, MITecco and MITigsm). MEDUSA1, MEDUSA2 and REcoM are three of
551 the four models with the longest residence times (decades to centuries, Table 2), relative to
552 the other FeMIP models, and produce high surface enrichment despite having some of the
553 lowest dust inputs (Table 2). For MEDUSA1 and MEDUSA2 the first order fixed scavenging
554 rate may be too low or have not enough variability to remove Fe rapidly when concentrations
555 are high. The constant Fe/C ratios used in these two models may also contribute to this
556 anomalous feature. In REcoM, Fe/C ratios are variable and the scavenging is second order, but
557 may simply be too low. DFe in TOPAZ has one of the shortest residence times (~8 years, Table
558 2), which implies that the surface accumulation of DFe may instead be linked to relatively
559 large sources or the variable ligand concentration. Since the ligand concentration in TOPAZ
560 depends on DOC, which typically decays from surface to deep, there may be too much DFe
561 stabilisation occurring in the surface ocean.

562

563 At intermediate depths, the inclusion of a prognostic Fe binding ligand pool with a particle
564 degradation source [Völker and Tagliabue, 2015] clearly improves the reproduction of
565 subsurface maxima in DFe associated with remineralisation (compare PISCES2 with PISCES1)
566 for many of the transects. Other models (COBALT and to a lesser degree BEC and BLING) are
567 able to reproduce these features but evidently do so for different reasons. These may be
568 related to the implicit formulation of particle flux (BEC) that ignores lateral transport of
569 particulate Fe or the shutdown of Fe scavenging in low oxygen conditions (BLING). It is
570 interesting that there appears to be two groups of subsurface DFe maxima seen in the
571 observations. Sometimes these features are tightly constrained to a small depth stratum (e.g.
572 equatorial ocean for GA-02, western margin on GA-03 and eastern margin on CoFeMUG),
573 while in other locations the DFe enrichments span almost the entire water column (eastern
574 margins on GA-03 and GP-16). Most models represent one or the other. For example,
575 subsurface maxima are always tightly bounded in depth for some models (e.g. COBALT and
576 PISCES2) or spread over depth in others (BEC) with no regional variations. Future work
577 should explore the potential mechanisms involved, which might be linked to subsurface
578 dissolution of dust, nutrient trapping or impacts of low oxygen. Emerging Fe isotope work
579 highlights the potential for non-reductive Fe release from margins [Conway and John, 2014;
580 Homoky et al., 2013] in addition to the role of reducing sediments represented in models.

581

582 In the ocean interior the best models (in terms of their linear correlation coefficients) are
583 those that include hydrothermal input (Table 3). While including such a source is clearly
584 important, it is possible that this is overemphasised in the correlations at the expense of other
585 deep ocean structure that is evident in many of the sections. For example, many of the ocean
586 sections do not show any 'watermass' related structure for DFe that is seen in macronutrients
587 (e.g. Figures 9 and 10). Although adding a hydrothermal ligand seems to improve the ability of
588 PISCES2 to reproduce the GP-16 data (Figure 7) and perhaps also the GA-02 hydrothermal
589 signal (Figure 4), it results in too widespread a hydrothermal anomaly in the Southern Ocean
590 (Figure 8) indicating too long a lifetime for this pool and the need for further refinement of
591 the processes governing hydrothermal Fe input [Tagliabue, 2014].

592

593 **4.2 Inter-Model differences in DFe inputs and cycling: the importance of scavenging**

594

595 It is notable that there is a great deal of variability in both the total Fe input flux (66.9 ± 67.1
596 Gmol Fe yr^{-1}) and the strength of a given source across the models, yet the mean ocean DFe is
597 strikingly similar ($0.58 \pm 0.14 \text{ nM}$). To a large extent, this agreement reflects the calibration of
598 scavenging rates and the concentration of organic ligands to obtain global average iron
599 concentrations in agreement with observations. While this relative homogeneity in modeled
600 mean DFe would be consistent with an earlier view of the oceanic Fe inventory [Johnson et al.,
601 1997], if anything, the emerging oceanic sections of DFe as part of the GEOTRACES
602 programme have highlighted an unexpected variability in DFe distributions in the ocean
603 interior [Mawji et al., 2015]. This is in stark contrast to the other main limiting nutrients,
604 which more closely reflect large-scale ocean circulation patterns and watermass related
605 features (e.g. Figures 9 and 10). Thus the apparent small differences in the mean ocean DFe
606 between models more likely arises from a modeling community that reflects an earlier
607 parsimonious view of the system. The relative constancy in the mean ocean DFe
608 concentrations in the models may reflect homogenous ligand concentrations of either 0.6 or
609 1.0 nM, but we note that even models with varying ligand concentrations (PISCES2 and
610 TOPAZ) show too much interior ocean uniformity.

611

612 In contrast to the mean DFe, there is a substantial degree of inter-model disagreement in the
613 strength of different sources. For instance, BFM, BLING, GENIE, MEDUSA1, MEDUSA2,
614 MITecco, MITigsm and REcoM all have atmospheric input fluxes of $< 5 \text{ Gmol Fe yr}^{-1}$, whereas
615 as in BEC, COBALT, PISCES1, PISCES2 and TOPAZ dust supply is much higher ($> 20 \text{ Gmol Fe}$
616 yr^{-1}). Yet this does not drive a similar trend in mean ocean DFe (with MITecco, MITigsm and
617 REcoM showing amongst the highest DFe concentrations, Table 2). We note that these
618 represent the total DFe flux from dust, accounting for model specific Fe mineralogy and
619 solubility. Equally, for those models that include sedimentary Fe input, this flux term can
620 range from very small (e.g. $< 5 \text{ Gmol Fe yr}^{-1}$ in MEDUSA2 or REcoM) to very large ($> 70 \text{ Gmol}$
621 Fe yr^{-1} in BEC, COBALT, MITecco, MITigsm and TOPAZ). Again this does not map onto mean
622 DFe trends. We note that the closer agreement for hydrothermal Fe input is more likely to
623 reflect the fact that only two models actually include this term, rather than greater confidence
624 regarding the actual flux. Overall, the total input of DFe does not explain the inter-model
625 variations found in mean DFe ($R^2=0.06$). This implies that there must be a great deal of
626 variability in how each model treats the scavenging of Fe in order to ultimately arrive at a
627 relatively similar mean ocean DFe concentration.

628
629 Most early Fe models that explicitly computed free Fe and sought to represent its scavenging
630 by sinking particles, treated the scavenging rate constant as a tunable parameter [Archer and
631 Johnson, 2000; Johnson *et al.*, 1997; Parekh *et al.*, 2004; Watson *et al.*, 2000]. This was viable in
632 these relatively simple box models against few observations, but is a less straightforward
633 solution for the multi tracer/process 3D biogeochemical models used presently where
634 scavenging itself maybe a function of other model parameters (e.g. particle concentrations)
635 and hence can vary considerably in space. Despite the long acknowledged influence of the
636 particle concentration on the scavenging rate [Honeyman *et al.*, 1988], a subset of the FeMIP
637 models persist with a globally uniform scavenging rate (Table 1). However, even for those
638 models that have implemented a second order scavenging rate, there is a question of how this
639 should operate. For example, should the model rely only on organic carbon or also include
640 biogenic silica and calcium carbonate? Non-biogenic particles, such as dust, as well as Fe and
641 manganese oxides, may also be important as Fe scavengers [Hayes *et al.*, 2015; Wagener *et al.*,
642 2008; Ye *et al.*, 2011]. There is also the important question of the specific affinity for free Fe
643 for these various carrier phases. Once Fe is scavenged onto particles, desorption of Fe will be
644 important in resupplying the DFe pool. Some models consider constant desorption rates
645 [Moore and Braucher, 2008], while others explicitly account for disaggregation dynamics and
646 the impact of bacterial activity [Aumont *et al.*, 2015]. Finally, there is the question of regional
647 and temporal variability in colloidal dynamics. Only some FeMIP models attempt to account
648 for this process (Table 1), yet given the apparent importance of colloidal Fe within the DFe
649 fraction [Boye *et al.*, 2010; Fitzsimmons and Boyle, 2014; Wu *et al.*, 2001], colloidal pumping
650 losses might be as large as those from the scavenging of free Fe. Some progress may be made
651 by exploiting the legacy from the field of Thorium (Th) cycling, for which a number of
652 different theories have been developed to describe its scavenging, including colloidal
653 components [Anderson, 2003; Burd *et al.*, 2000; Lam and Marchal, 2015; Marchal and Lam,
654 2012; Savoye *et al.*, 2006]. With an expanding database of paired Fe and Th observations,
655 including the particulate phase, as part of GEOTRACES [Mawji *et al.*, 2015] it may be possible
656 to refine this crucial component of the Fe cycle in the coming years.

657 658 **4.3 Impact of Fe on wider biogeochemical cycles: the importance of biological Fe cycling**

659
660 The biological cycling of DFe in a given model will dictate the net influence of a model's DFe
661 cycling on wider biogeochemical cycling and air-sea CO_2 exchange. In that regard, the large
662 oceanic sections, focused process studies and laboratory experiments all provide essential

663 and complementary information. For example, early laboratory studies demonstrated a large
664 degree of flexibility in the phytoplankton Fe/C ratios as a function of DFe levels and cell size,
665 as well as enhanced Fe/C ratios at lower light levels [*Sunda and Huntsman, 1997*]. Similar
666 ranges in Fe/C ratios are also seen in single cell analyses of phytoplankton from the ocean
667 [*Twining and Baines, 2013*]. The enhanced Fe/C ratio seen at low light is thought to reflect so-
668 called 'biodilution', where Fe uptake continues when phytoplankton carbon fixation is light
669 limited, and/or a greater absolute demand for Fe at low light [*Sunda and Huntsman, 1997*;
670 *Sunda and Huntsman, 1998*]. Almost all FeMIP models permit flexibility in the Fe/C ratio of
671 phytoplankton (Table 1), with those that consider Fe uptake independent of C fixation able to
672 account for any biodilution and the BLING model considers a direct impact of Fe on
673 photosynthesis. Emerging recent work has suggested that there are important inter-specific
674 differences in how phytoplankton Fe demands respond to light [*Strzepek et al., 2012*]. In their
675 laboratory study, *Strzepek et al. [2012]* found that while temperate diatom species indeed
676 showed elevated Fe/C ratios at low light, the opposite was true for Antarctic diatom species.
677 This raises questions about how models that generally do not consider different
678 phytoplankton species (but rather represent broader 'functional types') can account for these
679 potentially important regional distinctions in how environmental variations impact biological
680 Fe cycling.

681
682 Detailed process studies, mostly from the Southern Ocean, have sought to quantify Fe cycling
683 at the ecosystem level. In doing so, the importance of regenerated Fe in the fuelling of
684 biological productivity via the so-called 'ferrous wheel' has emerged as potentially important
685 [*Bowie et al., 2009; Bowie et al., 2015; Boyd et al., 2012; Boyd et al., 2005; Sarthou et al., 2008*;
686 *Strzepek et al., 2005*]. This has been demonstrated via the development of the 'fe-ratio', which
687 represents the proportion of Fe uptake from 'new' Fe sources. It has been determined for sites
688 across the Southern Ocean by assembling Fe budgets that combine measurements of Fe pools
689 and fluxes alongside laboratory estimates. The fe-ratio is generally around 0.1 (i.e. strongly
690 reliant on recycled Fe) in the low productivity regions of the Southern Ocean [*Bowie et al.,*
691 *2009; Boyd et al., 2005*] and reaches around 0.5 and greater (i.e. less reliant on recycled Fe) in
692 the naturally fertilised Kerguelen Island phytoplankton bloom [*Bowie et al., 2015; Sarthou et*
693 *al., 2008*]. Langrangian process studies have demonstrated a strong seasonal decline in the fe-
694 ratio as the spring phytoplankton bloom declines [*Boyd et al., 2012*], which are consistent
695 with low rates of Fe input during summer [*Tagliabue et al., 2014c*]. In agreement, direct
696 measurements of Fe fluxes between various components of the food web have highlighted
697 that only regenerative fluxes can support the measured Fe demand [*Boyd et al., 2012*;
698 *Strzepek et al., 2005; Tagliabue et al., 2014c*].

699
700 The sensitivity of a given model's biological productivity to new or regenerated forms of Fe is
701 crucial, as this will underpin its sensitivity to change. At present we do not know if the FeMIP
702 models place the correct emphases on new and recycled Fe in different ocean regions. Many
703 models rely on fixed rates of Fe regenerated by zooplankton and the remineralisation of
704 organic material, while others allow this to vary (Table 1). A key parameter in driving the
705 turnover of Fe by the zooplankton and bacterial communities in such models is an estimate of
706 the heterotroph demand for Fe, which is then balanced against the Fe/C provided as nutrition.
707 New measurements of stocks and turnover of Fe from specific ocean regions are also
708 beginning to emerge [*Boyd et al., 2015*], which will be invaluable in assessing the magnitude
709 and variability of the modelled rates.

710 711 **5. Future Work** 712

713 A weakness of the current intercomparison is that we did not truly intercompare the Fe
714 models, but instead compared the models' coupled physical-biogeochemical framework
715 (including Fe). This was necessary to retain as broad a suite of models as possible for this first
716 intercomparison. In future work, it would be useful to intercompare different Fe models
717 within the same physical model framework (e.g. as possible in the NEMO or MITgcm
718 modelling frameworks). Additionally, a set of planned model perturbations could be
719 performed where each individual model is subjected to a modification to its Fe supply (either
720 as a direct fertilisation event or by an alteration to one of the input fields). Much could be
721 learned from the way the Fe cycle responds to such perturbations across the different models.
722

723 Reducing uncertainty in the input fluxes of Fe is clearly important, but has proved difficult to
724 achieve over recent years (even for long recognised Fe sources such as dust). Some progress
725 could be made by implementing 'source specific' tracers (such as aluminium or manganese)
726 alongside Fe to constrain individual sources. Constraining scavenging rates has emerged as a
727 key priority and parallel simulation of Th may help constrain rates of Fe loss and the particle
728 pools. Moreover, many of the models used specifically for ecological questions are only run for
729 a few decades, leading to a greater sensitivity to initial conditions. A priority for such
730 'resource intensive' models would be the availability of input fields based on data
731 climatologies (such as those available for macronutrients as part of the World Ocean Atlas
732 datasets) or consensus distributions that may emerge from improved models.
733

734 As described in Sec. 4.3 an assessment of the different biological Fe models is also a priority,
735 as this will underpin the carbon cycle response and has not been compared against the
736 paradigms recently emerging from experimental work. A follow-up Phase of FeMIP could
737 include a closer comparison of the models against the detailed process study measurements
738 made (for example) as part of the FeCycle set of experiments [Boyd *et al.*, 2012; Boyd *et al.*,
739 2005]. A range of the Fe models could be set up in a one dimensional lagrangian framework
740 and forced by observed physics to be compared rigorously against the measured Fe stocks
741 and cycling rates.
742

743 **6. Conclusions**

744

745 We have compared the projected DFe distributions from thirteen global ocean
746 biogeochemistry models against each other and with available datasets. Newly-available full
747 depth sections of DFe collected from different oceanic regions as part of the GEOTRACES
748 programme have greatly facilitated this task. All models do relatively poorly in reproducing a
749 global DFe dataset of around 20,000 observations, which highlights the need for greater
750 understanding of how the ocean Fe cycle functions and how Fe should be represented in
751 global ocean models. We find a large degree of inter-model variability in the input fluxes of
752 DFe, which leads to great variability in the modeled residence times. The stronger inter-model
753 agreement in the mean ocean DFe most likely reflects earlier views of constant deep ocean
754 DFe levels maintained by a homogenous ligand pool and requires calibration via poorly
755 constrained scavenging rates. The way different models treat DFe scavenging has emerged as
756 a key uncertainty that would benefit from stronger observational constraints. More detailed
757 inter-model tests, particularly linked to process study data, are needed to assess the models'
758 biological components.
759

760 In closing, we re-emphasise the importance of the iron cycle in global ocean biogeochemistry
761 models, given its role, alongside NO_3 , as one of the two most important limiting nutrients.
762 Although the models analysed here struggle to capture the detailed distribution of this highly
763 dynamic element, it is very likely that biogeochemical models that include an iron cycle can

764 produce a more realistic simulation than models that do not. Improving the quantitative
765 understanding of iron cycling should be a major priority for ocean biogeochemistry research.
766

767

768

7. Acknowledgements

769

770 We thank everyone that has been involved in the development of the FeMIP ocean models
771 over many years. A.T especially thanks Eric Achterberg, Andrew Bowie, Maarten Klunder, Joe
772 Resing, Micha Rijkenberg, Mak Saito, Christian Schlosser and Peter Sedwick for sharing DFe
773 datasets ahead of their publication and Edward Mawji, Reiner Schlitzer, Elena Masferrer-
774 Dodas and the wider GEOTRACES community for their efforts in producing the Intermediate
775 Data Product (2014) that facilitated this inter comparison. PISCES1 and PISCES2 simulations
776 made use of the N8 HPC facilities, funded by the N8 consortium and EPSRC grant
777 EP/K000225/1. MV acknowledges the BFM system team (<http://bfm-community.eu>) for the
778 public availability of the BFM model. We thank Bob Anderson and Ric Williams for comments
779 on the draft manuscript and those of two anonymous reviewers that improved the final
780 version

781

782

8. References

783

784 Anderson, R. F. (2003), Chemical Tracers of Particle Transport, *Treatise on Geochemistry*, 247-
785 273. doi:10.1016/b0-08-043751-6/06111-9

786 Archer, D. E., and K. Johnson (2000), A model of the iron cycle in the ocean, *Global*
787 *Biogeochemical Cycles*, 14(1), 269-279. doi:10.1029/1999gb900053

788 Aumont, O., E. Maier-Reimer, S. Blain, and P. Monfray (2003), An ecosystem model of the
789 global ocean including Fe, Si, P colimitations, *Global Biogeochemical Cycles*, 17(2).
790 doi:10.1029/2001gb001745

791 Aumont, O., C. Ethé, A. Tagliabue, L. Bopp, and M. Gehlen (2015), PISCES-v2: an ocean
792 biogeochemical model for carbon and ecosystem studies, *Geoscientific Model Development*,
793 8(8), 2465-2513. doi:10.5194/gmd-8-2465-2015

794 Barbeau, K., J. W. Moffett, D. A. Caron, P. L. Croot, and D. L. Erdner (1996), Role of protozoan
795 grazing in relieving iron limitation of phytoplankton, *Nature*, 380(6569), 61-64.
796 doi:10.1038/380061a0

797 Bopp, L., et al. (2013), Multiple stressors of ocean ecosystems in the 21st century: projections
798 with CMIP5 models, *Biogeosciences*, 10(10), 6225-6245. doi:10.5194/bg-10-6225-2013

799 Bowie, A. R., D. Lannuzel, T. A. Remenyi, T. Wagener, P. J. Lam, P. W. Boyd, C. Guieu, A. T.
800 Townsend, and T. W. Trull (2009), Biogeochemical iron budgets of the Southern Ocean south
801 of Australia: Decoupling of iron and nutrient cycles in the subantarctic zone by the
802 summertime supply, *Global Biogeochemical Cycles*, 23(4). doi:10.1029/2009gb003500

803 Bowie, A. R., et al. (2015), Iron budgets for three distinct biogeochemical sites around the
804 Kerguelen Archipelago (Southern Ocean) during the natural fertilisation study, KEOPS-2,
805 *Biogeosciences*, 12(14), 4421-4445. doi:10.5194/bg-12-4421-2015

806 Boyd, P. W., and M. J. Ellwood (2010), The biogeochemical cycle of iron in the ocean, *Nature*
807 *Geoscience*, 3(10), 675-682. doi:10.1038/ngeo964

808 Boyd, P. W., R. F. Strzepek, M. J. Ellwood, D. A. Hutchins, S. D. Nodder, B. S. Twining, and S. W.
809 Wilhelm (2015), Why are biotic iron pools uniform across high- and low-iron pelagic
810 ecosystems?, *Global Biogeochemical Cycles*, 29(7), 1028-1043. doi:10.1002/2014gb005014

811 Boyd, P. W., et al. (2012), Microbial control of diatom bloom dynamics in the open ocean,
812 *Geophysical Research Letters*, 39(18). doi:10.1029/2012gl053448

813 Boyd, P. W., et al. (2005), FeCycle: Attempting an iron biogeochemical budget from a
814 mesoscale SF6 tracer experiment in unperturbed low iron waters, *Global Biogeochemical*
815 *Cycles*, 19(4). doi:10.1029/2005gb002494

816 Boye, M., J. Nishioka, P. Croot, P. Laan, K. R. Timmermans, V. H. Strass, S. Takeda, and H. J. W.
817 de Baar (2010), Significant portion of dissolved organic Fe complexes in fact is Fe colloids,
818 *Marine Chemistry*, 122(1-4), 20-27. doi:10.1016/j.marchem.2010.09.001

819 Bruland, K. W., R. Middag, and M. C. Lohan (2014), Controls of Trace Metals in Seawater,
820 *Treatise on Geochemistry, 2nd edition*, 19-51. doi:10.1016/b978-0-08-095975-7.00602-1

821 Burd, A. B., S. B. Moran, and G. A. Jackson (2000), A coupled adsorption–aggregation model of
822 the POC/ ratio of marine particles, *Deep Sea Research Part I: Oceanographic Research Papers*,
823 47(1), 103-120. doi:10.1016/s0967-0637(99)00047-3

824 Chever, F., E. Bucciarelli, G. Sarthou, S. Speich, M. Arhan, P. Penven, and A. Tagliabue (2010),
825 Physical speciation of iron in the Atlantic sector of the Southern Ocean along a transect from
826 the subtropical domain to the Weddell Sea Gyre, *J Geophys Res-Oceans*, 115(C10).
827 doi:10.1029/2009jc005880

828 Conway, T. M., and S. G. John (2014), Quantification of dissolved iron sources to the North
829 Atlantic Ocean, *Nature*, 511(7508), 212-215. doi:10.1038/nature13482

830 Dunne, J. P., et al. (2013), GFDL’s ESM2 Global Coupled Climate–Carbon Earth System Models.
831 Part II: Carbon System Formulation and Baseline Simulation Characteristics*, *Journal of*
832 *Climate*, 26(7), 2247-2267. doi:10.1175/jcli-d-12-00150.1

833 Dutkiewicz, S., J. R. Scott, and M. J. Follows (2013), Winners and losers: Ecological and
834 biogeochemical changes in a warming ocean, *Global Biogeochemical Cycles*, 27(2), 463-477.
835 doi:10.1002/gbc.20042

836 Dutkiewicz, S., B. A. Ward, F. Monteiro, and M. J. Follows (2012), Interconnection of nitrogen
837 fixers and iron in the Pacific Ocean: Theory and numerical simulations, *Global Biogeochemical*
838 *Cycles*, 26(1). doi:10.1029/2011gb004039

839 Dutkiewicz, S., B. A. Ward, J. R. Scott, and M. J. Follows (2014), Understanding predicted shifts
840 in diazotroph biogeography using resource competition theory, *Biogeosciences*, 11(19), 5445-
841 5461. doi:10.5194/bg-11-5445-2014

842 Dutkiewicz, S., A. E. Hickman, O. Jahn, W. W. Gregg, C. B. Mouw, and M. J. Follows (2015),
843 Capturing optically important constituents and properties in a marine biogeochemical and
844 ecosystem model, *Biogeosciences*, 12(14), 4447-4481. doi:10.5194/bg-12-4447-2015

845 Elrod, V. A., W. M. Berelson, K. H. Coale, and K. S. Johnson (2004), The flux of iron from
846 continental shelf sediments: A missing source for global budgets, *Geophysical Research Letters*,
847 31(12). doi:10.1029/2004gl020216

- 848 Fitzsimmons, J. N., and E. A. Boyle (2014), Both soluble and colloidal iron phases control
849 dissolved iron variability in the tropical North Atlantic Ocean, *Geochimica et Cosmochimica*
850 *Acta*, 125, 539-550. doi:10.1016/j.gca.2013.10.032
- 851 Frew, R. D., D. A. Hutchins, S. Nodder, S. Sanudo-Wilhelmy, A. Tovar-Sanchez, K. Leblanc, C. E.
852 Hare, and P. W. Boyd (2006), Particulate iron dynamics during FeCycle in subantarctic waters
853 southeast of New Zealand, *Global Biogeochemical Cycles*, 20(1). doi:10.1029/2005gb002558
- 854 Galbraith, E. D., A. Gnanadesikan, J. P. Dunne, and M. R. Hiscock (2010), Regional impacts of
855 iron-light colimitation in a global biogeochemical model, *Biogeosciences*, 7(3), 1043-1064.
856 doi:10.5194/bg-7-1043-2010
- 857 Gerringa, L. J. A., A. C. Alderkamp, P. Laan, C. E. Thuroczy, H. J. W. De Baar, M. M. Mills, G. L. van
858 Dijken, H. van Haren, and K. R. Arrigo (2012), Iron from melting glaciers fuels the
859 phytoplankton blooms in Amundsen Sea (Southern Ocean): Iron biogeochemistry, *Deep-Sea*
860 *Res Pt II*, 71-76, 16-31. doi:Doi 10.1016/J.Dsr2.2012.03.007
- 861 Gledhill, M., and K. N. Buck (2012), The organic complexation of iron in the marine
862 environment: a review, *Frontiers in microbiology*, 3, 69. doi:10.3389/fmicb.2012.00069
- 863 Hatta, M., C. I. Measures, J. Wu, S. Roshan, J. N. Fitzsimmons, P. Sedwick, and P. Morton (2014),
864 An overview of dissolved Fe and Mn Distributions during the 2010–2011 U.S. GEOTRACES
865 north Atlantic Cruises: GEOTRACES GA03, *Deep Sea Research Part II: Topical Studies in*
866 *Oceanography*. doi:10.1016/j.dsr2.2014.07.005
- 867 Hauck, J., C. Völker, T. Wang, M. Hoppema, M. Losch, and D. A. Wolf-Gladrow (2013),
868 Seasonally different carbon flux changes in the Southern Ocean in response to the southern
869 annular mode, *Global Biogeochemical Cycles*, 27(4), 1236-1245. doi:10.1002/2013gb004600
- 870 Hayes, C. T., et al. (2015), Intensity of Th and Pa scavenging partitioned by particle chemistry
871 in the North Atlantic Ocean, *Marine Chemistry*, 170, 49-60.
872 doi:10.1016/j.marchem.2015.01.006
- 873 Homoky, W. B., S. G. John, T. M. Conway, and R. A. Mills (2013), Distinct iron isotopic
874 signatures and supply from marine sediment dissolution, *Nature communications*, 4, 2143.
875 doi:10.1038/ncomms3143
- 876 Honeyman, B. D., and P. H. Santschi (1989), A Brownian-pumping model for oceanic trace
877 metal scavenging: Evidence from Th isotopes, *Journal of Marine Research*, 47(4), 951-992.
878 doi:10.1357/002224089785076091
- 879 Honeyman, B. D., L. S. Balistrieri, and J. W. Murray (1988), Oceanic trace metal scavenging: the
880 importance of particle concentration, *Deep Sea Research Part A. Oceanographic Research*
881 *Papers*, 35(2), 227-246. doi:10.1016/0198-0149(88)90038-6
- 882 Hutchins, D. A., and K. W. Bruland (1994), Grazer-Mediated Regeneration and Assimilation of
883 Fe, Zn and Mn from Planktonic Prey, *Marine Ecology Progress Series*, 110(2-3), 259-269.
884 doi:Doi 10.3354/Meps110259
- 885 Jickells, T. D., et al. (2005), Global iron connections between desert dust, ocean
886 biogeochemistry, and climate, *Science*, 308(5718), 67-71. doi:10.1126/Science.1105959

- 887 Johnson, K. S., R. M. Gordon, and K. H. Coale (1997), What controls dissolved iron
888 concentrations in the world ocean?, *Marine Chemistry*, 57(3-4), 137-161. doi:10.1016/s0304-
889 4203(97)00043-1
- 890 Klunder, M. B., P. Laan, R. Middag, H. J. W. De Baar, and J. C. van Ooijen (2011), Dissolved iron
891 in the Southern Ocean (Atlantic sector), *Deep Sea Research Part II: Topical Studies in*
892 *Oceanography*, 58(25-26), 2678-2694. doi:10.1016/j.dsr2.2010.10.042
- 893 Kohfeld, K. E., and A. Ridgwell (2009), Glacial-Interglacial Variability in Atmospheric CO₂,
894 *Surface Ocean--Lower Atmosphere Processes*, 187, 251-286. doi:10.1029/2008gm000845
- 895 Lam, P. J., and O. Marchal (2015), Insights into particle cycling from thorium and particle data,
896 *Annual review of marine science*, 7, 159-184. doi:10.1146/annurev-marine-010814-015623
- 897 Lefèvre, N., and A. J. Watson (1999), Modeling the geochemical cycle of iron in the oceans and
898 its impact on atmospheric CO₂ concentrations, *Global Biogeochemical Cycles*, 13(3), 727-736.
899 doi:10.1029/1999gb900034
- 900 Liu, X., and F. J. Millero (1999), The solubility of iron hydroxide in sodium chloride solutions,
901 *Geochimica et Cosmochimica Acta*, 63(19-20), 3487-3497. doi:10.1016/s0016-
902 7037(99)00270-7
- 903 Marchal, O., and P. J. Lam (2012), What can paired measurements of Th isotope activity and
904 particle concentration tell us about particle cycling in the ocean?, *Geochimica et Cosmochimica*
905 *Acta*, 90, 126-148. doi:10.1016/j.gca.2012.05.009
- 906 Marchetti, A., M. S. Parker, L. P. Moccia, E. O. Lin, A. L. Arrieta, F. Ribalet, M. E. Murphy, M. T.
907 Maldonado, and E. V. Armbrust (2009), Ferritin is used for iron storage in bloom-forming
908 marine pennate diatoms, *Nature*, 457(7228), 467-470. doi:10.1038/nature07539
- 909 Matsumoto, K., K. Tokos, A. Huston, and H. Joy-Warren (2013), MESMO 2: a mechanistic
910 marine silica cycle and coupling to a simple terrestrial scheme, *Geoscientific Model*
911 *Development*, 6(2), 477-494. doi:10.5194/gmd-6-477-2013
- 912 Mawji, E., R. Schlitzer, E. Masferrer-Dodas, and GEOTRACES-group (2015), The GEOTRACES
913 Intermediate Data Product 2014, *Marine Chemistry*. doi:10.1016/j.marchem.2015.04.005
- 914 Misumi, K., K. Lindsay, J. K. Moore, S. C. Doney, D. Tsumune, and Y. Yoshida (2013), Humic
915 substances may control dissolved iron distributions in the global ocean: Implications from
916 numerical simulations, *Global Biogeochemical Cycles*, 27(2), 450-462. doi:10.1002/gbc.20039
- 917 Moore, C. M., et al. (2013), Processes and patterns of oceanic nutrient limitation, *Nature*
918 *Geoscience*. doi:10.1038/ngeo1765
- 919 Moore, J. K., and O. Braucher (2008), Sedimentary and mineral dust sources of dissolved iron
920 to the world ocean, *Biogeosciences*, 5(3), 631-656. doi:10.5194/bg-5-631-2008
- 921 Moore, J. K., S. C. Doney, D. M. Glover, and I. Y. Fung (2002), Iron cycling and nutrient-
922 limitation patterns in surface waters of the World Ocean, *Deep-Sea Res Pt II*, 49(1-3), 463-507.
923 doi:10.1016/S0967-0645(01)00109-6
- 924 Moore, J. K., K. Lindsay, S. C. Doney, M. C. Long, and K. Misumi (2013), Marine Ecosystem
925 Dynamics and Biogeochemical Cycling in the Community Earth System Model [CESM1(BGC)]:

- 926 Comparison of the 1990s with the 2090s under the RCP4.5 and RCP8.5 Scenarios, *Journal of*
927 *Climate*, 26(23), 9291-9312. doi:10.1175/jcli-d-12-00566.1
- 928 Noble, A. E., et al. (2012), Basin-scale inputs of cobalt, iron, and manganese from the
929 Benguela-Angola front to the South Atlantic Ocean, *Limnology and Oceanography*, 57(4), 989-
930 1010. doi:10.4319/lo.2012.57.4.0989
- 931 Parekh, P., M. J. Follows, and E. Boyle (2004), Modeling the global ocean iron cycle, *Global*
932 *Biogeochemical Cycles*, 18(1). doi:10.1029/2003gb002061
- 933 Raiswell, R., L. G. Benning, M. Tranter, and S. Tulaczyk (2008), Bioavailable iron in the
934 Southern Ocean: the significance of the iceberg conveyor belt, *Geochemical transactions*, 9, 7.
935 doi:10.1186/1467-4866-9-7
- 936 Raven, J. A. (1988), The iron and molybdenum use efficiencies of plant growth with different
937 energy, carbon and nitrogen sources, *New Phytologist*, 109(3), 279-287. doi:10.1111/j.1469-
938 8137.1988.tb04196.x
- 939 Raven, J. A., M. C. W. Evans, and R. E. Korb (1999), The role of trace metals in photosynthetic
940 electron transport in O₂-evolving organisms, *Photosynthesis research*, 60(2/3), 111-150.
941 doi:10.1023/a:1006282714942
- 942 Resing, J. A., P. N. Sedwick, C. R. German, W. Jenkins, J. W. Moffett, B. Sohst, and A. Tagliabue
943 (2015), Basin-scale transport of hydrothermal dissolved metals across the South Pacific
944 Ocean, *Nature*. doi:10.1038/nature14577
- 945 Ridgwell, A. J. (2001), Glacial-interglacial perturbations in the global carbon cycle, University
946 of East Anglia.
- 947 Rijkenberg, M. J., R. Middag, P. Laan, L. J. Gerringa, H. M. van Aken, V. Schoemann, J. T. de Jong,
948 and H. J. de Baar (2014), The distribution of dissolved iron in the west atlantic ocean, *Plos One*,
949 9(6), e101323. doi:10.1371/journal.pone.0101323
- 950 Saito, M. A., A. E. Noble, A. Tagliabue, T. J. Goepfert, C. H. Lamborg, and W. J. Jenkins (2013),
951 Slow-spreading submarine ridges in the South Atlantic as a significant oceanic iron source,
952 *Nature Geoscience*, 6(9), 775-779. doi:10.1038/Ngeo1893
- 953 Sarthou, G., D. Vincent, U. Christaki, I. Obernosterer, K. R. Timmermans, and C. P. D. Brussaard
954 (2008), The fate of biogenic iron during a phytoplankton bloom induced by natural
955 fertilisation: Impact of copepod grazing, *Deep Sea Research Part II: Topical Studies in*
956 *Oceanography*, 55(5-7), 734-751. doi:10.1016/j.dsr2.2007.12.033
- 957 Savoye, N., C. Benitez-Nelson, A. B. Burd, J. K. Cochran, M. Charette, K. O. Buesseler, G. A.
958 Jackson, M. Roy-Barman, S. Schmidt, and M. Elskens (2006), ²³⁴Th sorption and export
959 models in the water column: A review, *Marine Chemistry*, 100(3-4), 234-249.
960 doi:10.1016/j.marchem.2005.10.014
- 961 Stock, C. A., J. P. Dunne, and J. G. John (2014), Global-scale carbon and energy flows through
962 the marine planktonic food web: An analysis with a coupled physical-biological model,
963 *Progress in Oceanography*, 120, 1-28. doi:10.1016/j.pcean.2013.07.001

- 964 Strzepek, R. F., K. A. Hunter, R. D. Frew, P. J. Harrison, and P. W. Boyd (2012), Iron-light
965 interactions differ in Southern Ocean phytoplankton, *Limnology and Oceanography*, 57(4),
966 1182-1200. doi:10.4319/lo.2012.57.4.1182
- 967 Strzepek, R. F., M. T. Maldonado, J. L. Higgins, J. Hall, K. Safi, S. W. Wilhelm, and P. W. Boyd
968 (2005), Spinning the “Ferrous Wheel”: The importance of the microbial community in an iron
969 budget during the FeCycle experiment, *Global Biogeochemical Cycles*, 19(4), GB4S26.
970 doi:10.1029/2005gb002490
- 971 Sunda, W. G., and S. A. Huntsman (1997), Interrelated influence of iron, light and cell size on
972 marine phytoplankton growth, *Nature*, 390(6658), 389-392. doi:10.1038/37093
- 973 Sunda, W. G., and S. A. Huntsman (1998), Processes regulating cellular metal accumulation
974 and physiological effects: Phytoplankton as model systems, *Science of The Total Environment*,
975 219(2-3), 165-181. doi:10.1016/s0048-9697(98)00226-5
- 976 Tagliabue, A. (2014), More to hydrothermal iron input than meets the eye, *Proceedings of the*
977 *National Academy of Sciences of the United States of America*, 111(47), 16641-16642.
978 doi:10.1073/pnas.1419829111
- 979 Tagliabue, A., and C. Völker (2011), Towards accounting for dissolved iron speciation in global
980 ocean models, *Biogeosciences*, 8(10), 3025-3039. doi:10.5194/bg-8-3025-2011
- 981 Tagliabue, A., L. Bopp, and O. Aumont (2008), Ocean biogeochemistry exhibits contrasting
982 responses to a large scale reduction in dust deposition, *Biogeosciences*, 5(1), 11-24.
- 983 Tagliabue, A., O. Aumont, and L. Bopp (2014a), The impact of different external sources of iron
984 on the global carbon cycle, *Geophysical Research Letters*, 41(3), 920-926.
985 doi:10.1002/2013gl059059
- 986 Tagliabue, A., R. G. Williams, N. Rogan, E. P. Achterberg, and P. W. Boyd (2014b), A ventilation-
987 based framework to explain the regeneration-scavenging balance of iron in the ocean,
988 *Geophysical Research Letters*, 41(20), 7227-7236. doi:10.1002/2014gl061066
- 989 Tagliabue, A., J.-B. Sallée, A. R. Bowie, M. Lévy, S. Swart, and P. W. Boyd (2014c), Surface-water
990 iron supplies in the Southern Ocean sustained by deep winter mixing, *Nature Geoscience*, 7(4),
991 314-320. doi:10.1038/ngeo2101
- 992 Tagliabue, A., T. Mtshali, O. Aumont, A. R. Bowie, M. B. Klunder, A. N. Roychoudhury, and S.
993 Swart (2012), A global compilation of dissolved iron measurements: focus on distributions
994 and processes in the Southern Ocean, *Biogeosciences*, 9(6), 2333-2349. doi:10.5194/bg-9-
995 2333-2012
- 996 Tagliabue, A., L. Bopp, D. M. Roche, N. Bouttes, J. C. Dutay, R. Alkama, M. Kageyama, E. Michel,
997 and D. Paillard (2009), Quantifying the roles of ocean circulation and biogeochemistry in
998 governing ocean carbon-13 and atmospheric carbon dioxide at the last glacial maximum,
999 *Climate of the Past*, 5(4), 695-706. doi:10.5194/cp-5-695-2009
- 1000 Tagliabue, A., et al. (2010), Hydrothermal contribution to the oceanic dissolved iron
1001 inventory, *Nature Geoscience*, 3(4), 252-256. doi:10.1038/ngeo818
- 1002 Twining, B. S., and S. B. Baines (2013), The trace metal composition of marine phytoplankton,
1003 *Annual review of marine science*, 5, 191-215. doi:10.1146/annurev-marine-121211-172322

- 1004 Twining, B. S., S. D. Nodder, A. L. King, D. A. Hutchins, G. R. LeCleir, J. M. DeBruyn, E. W. Maas, S.
1005 Vogt, S. W. Wilhelm, and P. W. Boyd (2014), Differential remineralization of major and trace
1006 elements in sinking diatoms, *Limnol. Oceanogr*, 59(3), 689-704.
1007 doi:10.4319/lo.2014.59.3.0689
- 1008 Vichi, M., N. Pinardi, and S. Masina (2007), A generalized model of pelagic biogeochemistry for
1009 the global ocean ecosystem. Part I: Theory, *Journal of Marine Systems*, 64(1-4), 89-109.
1010 doi:10.1016/j.jmarsys.2006.03.006
- 1011 Völker, C., and A. Tagliabue (2015), Modeling organic iron-binding ligands in a three-
1012 dimensional biogeochemical ocean model, *Marine Chemistry*, 173, 67-77.
1013 doi:10.1016/j.marchem.2014.11.008
- 1014 Wagener, T., E. Pulido-Villena, and C. Guieu (2008), Dust iron dissolution in seawater: Results
1015 from a one-year time-series in the Mediterranean Sea, *Geophysical Research Letters*, 35(16).
1016 doi:10.1029/2008gl034581
- 1017 Ward, B. A., S. Dutkiewicz, C. M. Moore, and M. J. Follows (2013), Iron, phosphorus, and
1018 nitrogen supply ratios define the biogeography of nitrogen fixation, *Limnology and
1019 Oceanography*, 58(6), 2059-2075. doi:10.4319/lo.2013.58.6.2059
- 1020 Watson, A. J., D. C. E. Bakker, A. J. Ridgwell, P. W. Boyd, and C. S. Law (2000), Effect of iron
1021 supply on Southern Ocean CO₂ uptake and implications for glacial atmospheric CO₂, *Nature*,
1022 407(6805), 730-733. doi:10.1038/35037561
- 1023 Wells, M. L., N. M. Price, and K. W. Bruland (1995), Iron chemistry in seawater and its
1024 relationship to phytoplankton: a workshop report, *Marine Chemistry*, 48(2), 157-182.
1025 doi:10.1016/0304-4203(94)00055-i
- 1026 Wu, J., E. Boyle, W. Sunda, and L. S. Wen (2001), Soluble and colloidal iron in the oligotrophic
1027 North Atlantic and North Pacific, *Science*, 293(5531), 847-849. doi:10.1126/science.1059251
- 1028 Ye, Y., T. Wagener, C. Völker, C. Guieu, and D. A. Wolf-Gladrow (2011), Dust deposition: iron
1029 source or sink? A case study, *Biogeosciences*, 8(8), 2107-2124. doi:10.5194/bg-8-2107-2011
- 1030 Yool, A., E. E. Popova, and T. R. Anderson (2011), Medusa-1.0: a new intermediate complexity
1031 plankton ecosystem model for the global domain, *Geoscientific Model Development*, 4(2), 381-
1032 417. doi:10.5194/gmd-4-381-2011
- 1033 Yool, A., E. E. Popova, and T. R. Anderson (2013), MEDUSA-2.0: an intermediate complexity
1034 biogeochemical model of the marine carbon cycle for climate change and ocean acidification
1035 studies, *Geoscientific Model Development*, 6(5), 1767-1811. doi:10.5194/gmd-6-1767-2013
1036
- 1037 **Figure Legends**
1038
- 1039 **Figure 1.** Histograms of the average DFe concentration (nM) simulated by the FeMIP models
1040 across four different depth bins for three regions. The Northern Hemisphere is 30°N-90°N,
1041 Tropics are 30°S-30°N and the Southern Hemisphere is 30°S-90°S.
1042
- 1043 **Figure 2.** Annual mean DFe concentrations (nM) averaged over the upper 50m from the
1044 FeMIP models. Data averaged over the period January to June and July to December is taken
1045 from the expanded Tagliabue *et al.* [2012] dataset and has been averaged over 5° bins in
1046 latitude and longitude to improve visibility.

1047

1048 **Figure 3.** Annual maximum minus annual minimum DFe concentrations (nM) averaged over
1049 the upper 50m from the FeMIP models.

1050

1051 **Figure 4.** DFe concentrations (nM) from the GA-02 [Rijkenberg *et al.*, 2014] cruise and
1052 extracted from the FeMIP models.

1053

1054 **Figure 5.** DFe concentrations (nM) from the GA-03 cruise [Hatta *et al.*, 2014] and extracted
1055 from the FeMIP models.

1056

1057 **Figure 6.** DFe concentrations (nM) from the CoFeMUG cruise [Noble *et al.*, 2012] and
1058 extracted from the FeMIP models.

1059

1060 **Figure 7.** DFe concentrations (nM) from the GP-16 cruise [Resing *et al.*, 2015] and extracted
1061 from the FeMIP models.

1062

1063 **Figure 8.** DFe concentrations (nM) from the GIPY-4 and 5 cruises [Chever *et al.*, 2010; Klunder
1064 *et al.*, 2011] and extracted from the FeMIP models

1065

1066 **Figure 9.** NO₃ concentrations (μM) from the GA-02 cruise [Rijkenberg *et al.*, 2014] and
1067 extracted from the FeMIP models (NO₃ data not provided for GENIE).

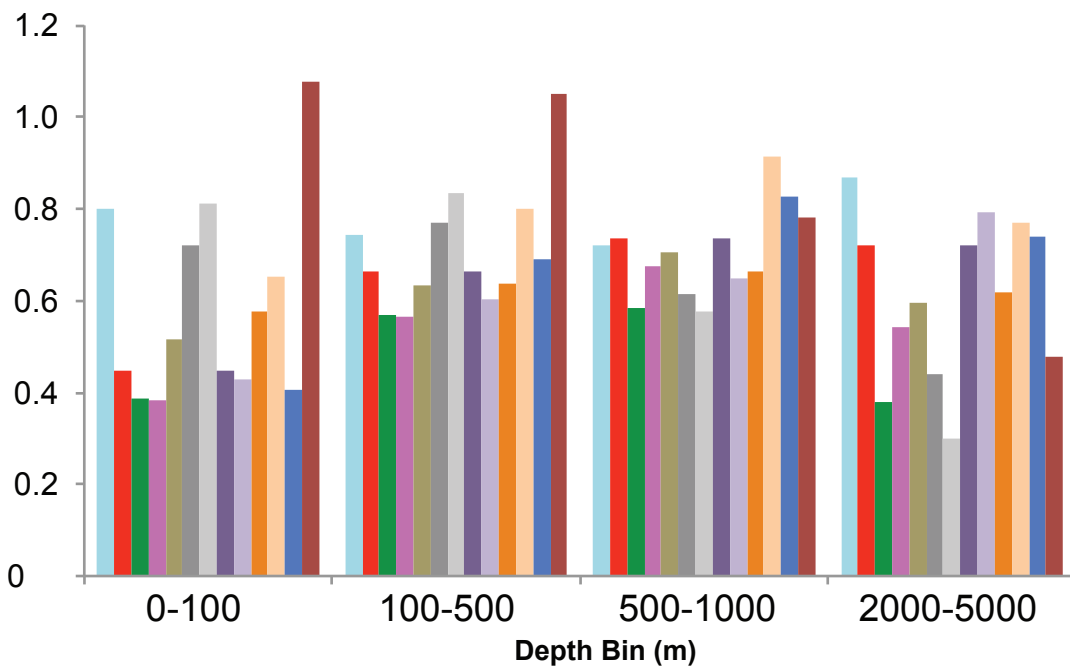
1068

1069 **Figure 10.** PO₄ concentrations (μM) from the GA-02 cruise [Rijkenberg *et al.*, 2014] and
1070 extracted from the FeMIP models (PO₄ not provided for MEDUSA-1, MEDUSA-2, RECOM and
1071 TOPAZ).

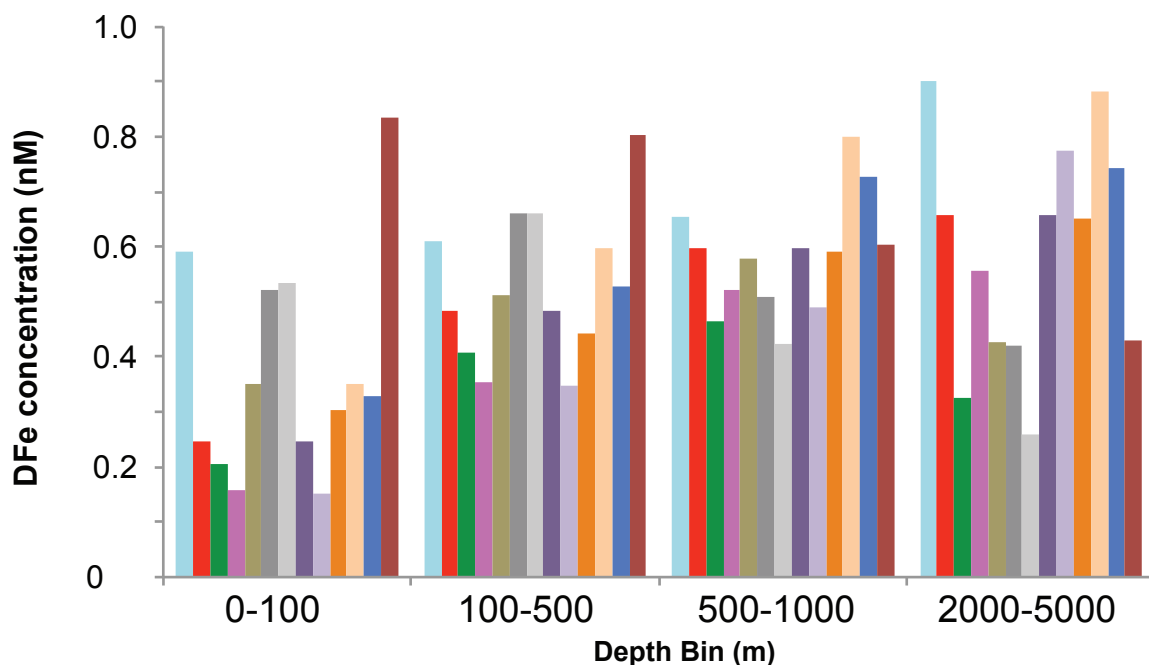
1072

1073 **Figure 11.** Fe* (Fe - NO₃*r_{Fe/N}, nM) from the GA-02 cruise [Rijkenberg *et al.*, 2014] and
1074 extracted from the FeMIP models. For models that do not provide NO₃, PO₄ is used and
1075 converted to NO₃ assuming a ratio of 16:1.

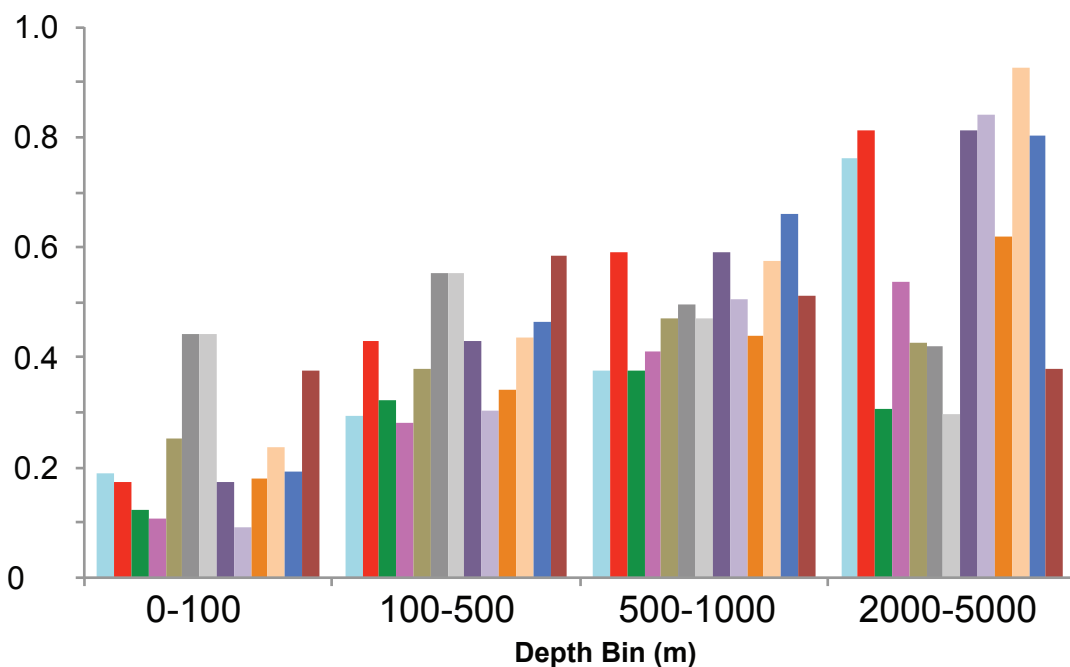
Northern Hemisphere



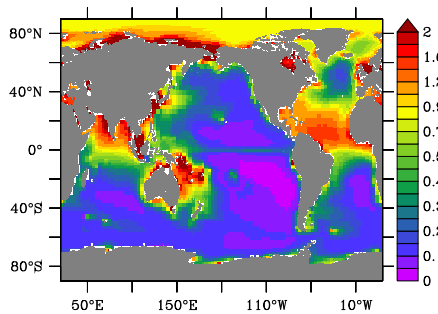
Tropics



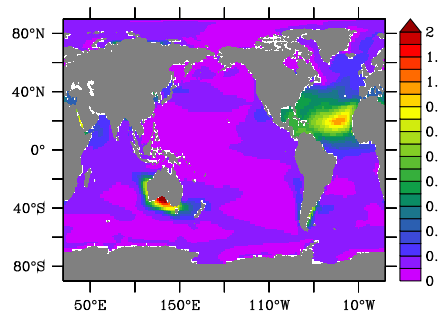
Southern Hemisphere



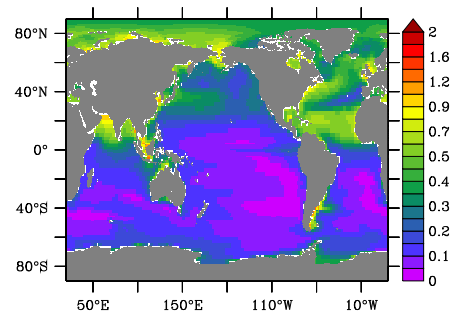
BEC



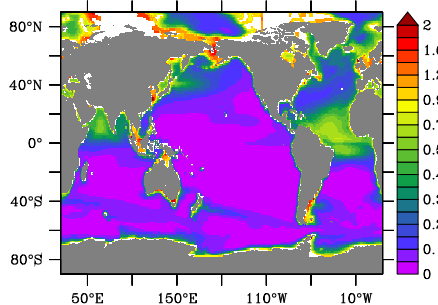
BFM



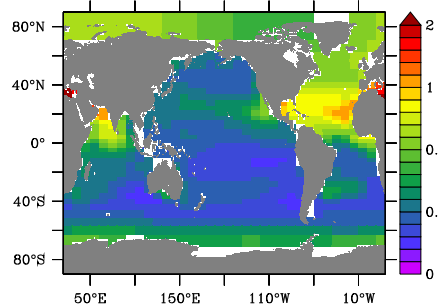
BLING



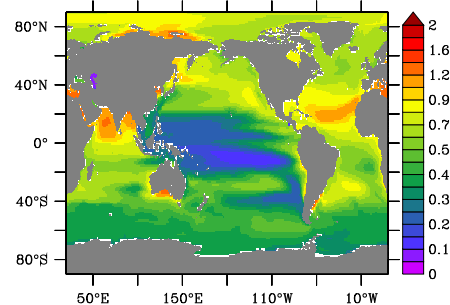
COBALT



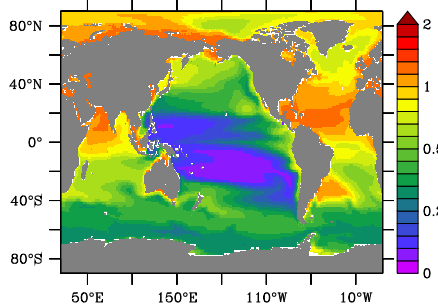
GENIE



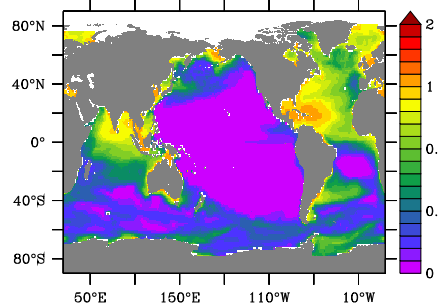
MEDUSA 1



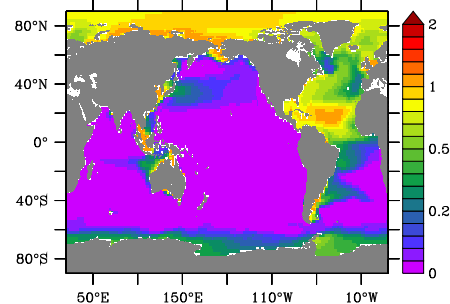
MEDUSA 2



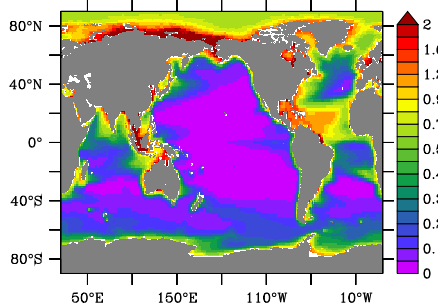
MIT ecco



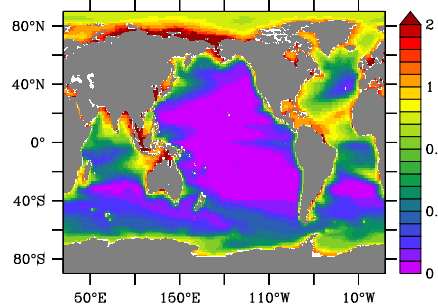
MIT igsm



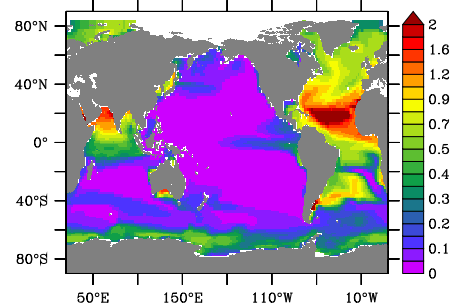
PISCES 1



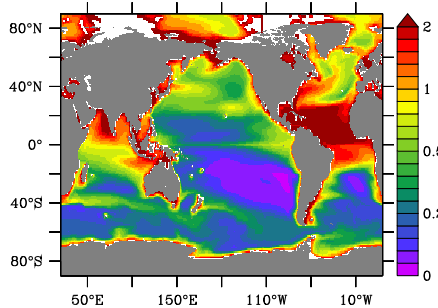
PISCES 2



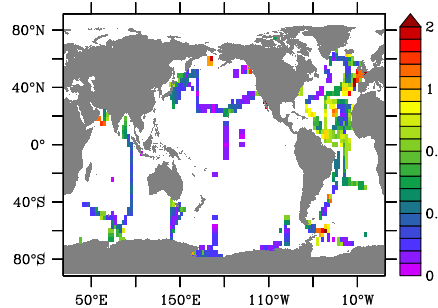
RECOM



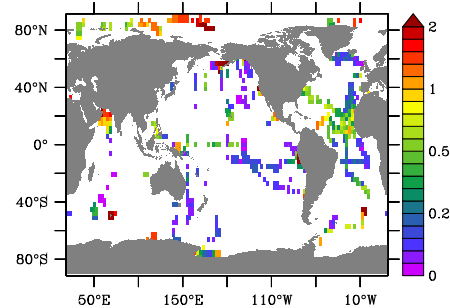
TOPAZ



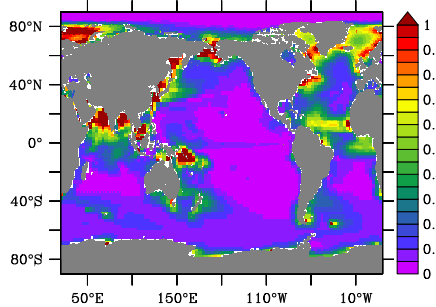
Data, Jan to Jun



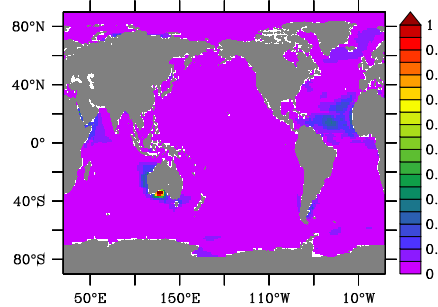
Data, Jul to Dec



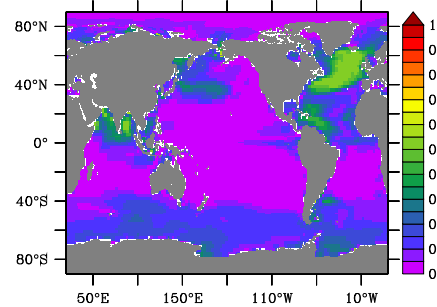
BEC



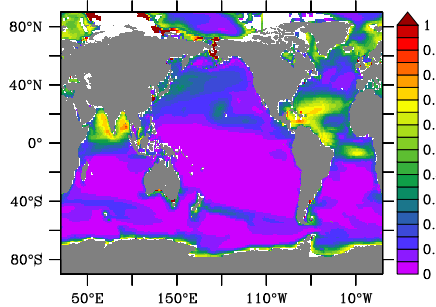
BFM



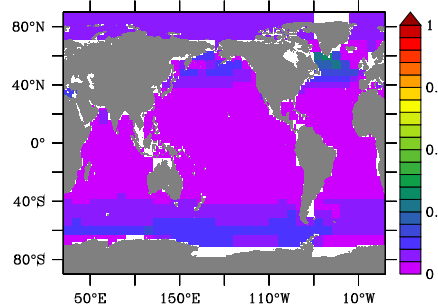
BLING



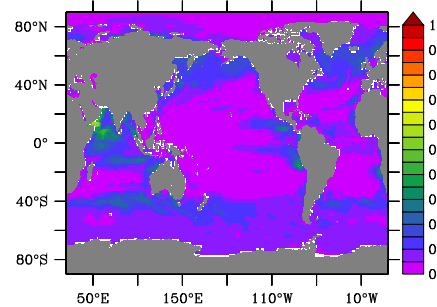
COBALT



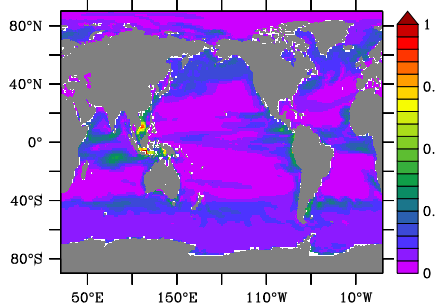
GENIE



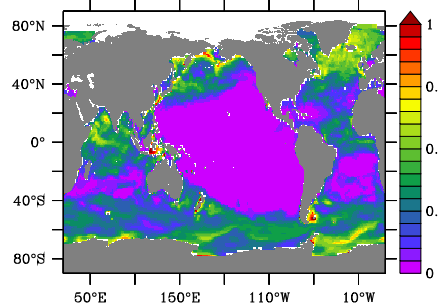
MEDUSA 1



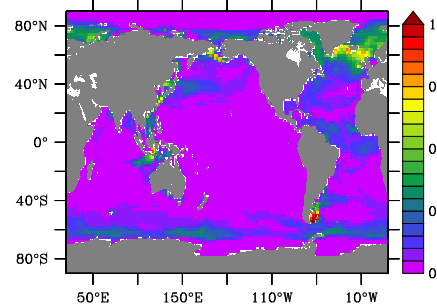
MEDUSA 2



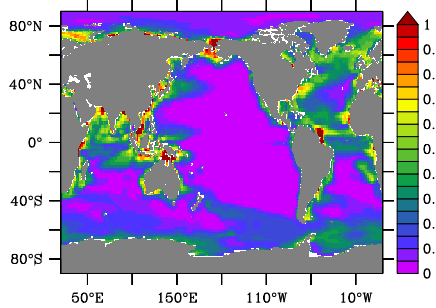
MIT ecco



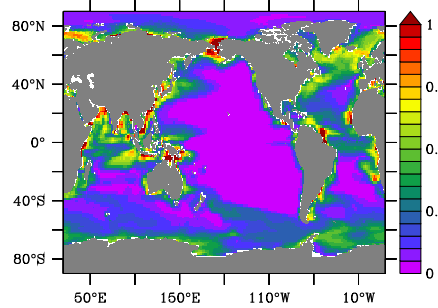
MIT igsm



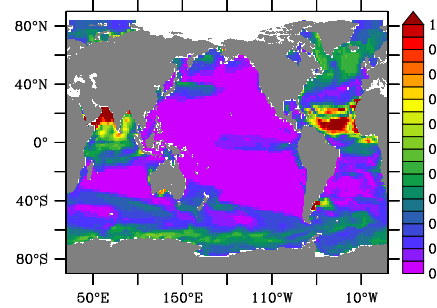
PISCES 1



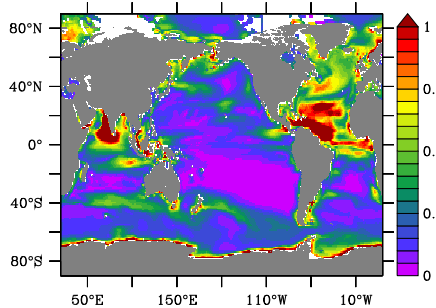
PISCES 2



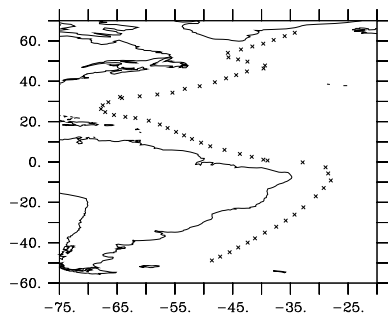
RECOM



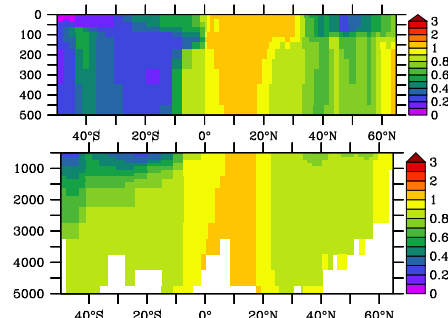
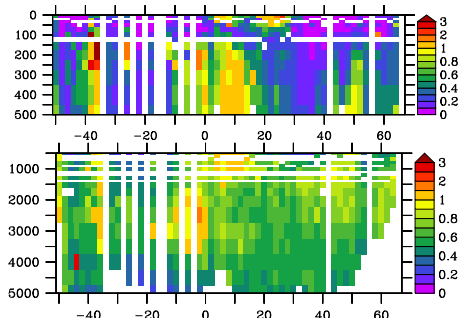
TOPAZ



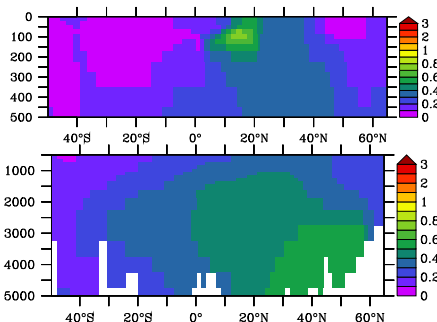
GA-02, Cruise



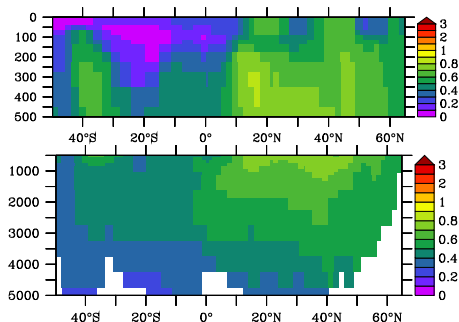
BEC, GA-02



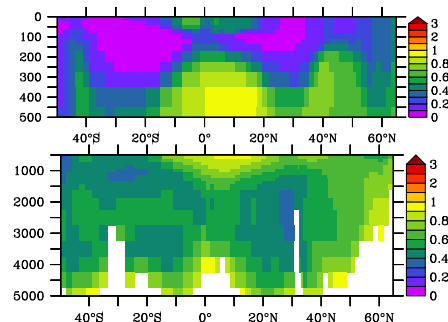
BFM, GA-02



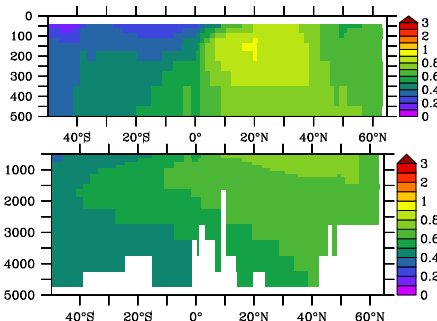
BLING, GA-02



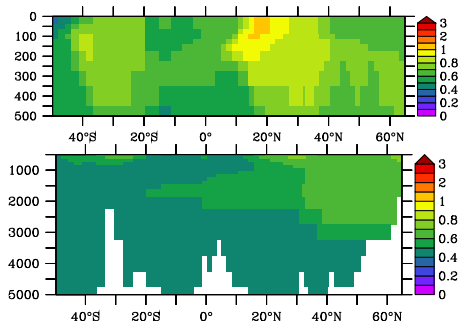
COBALT, GA-02



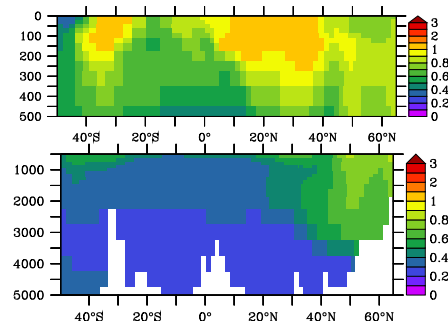
GENIE, GA-02



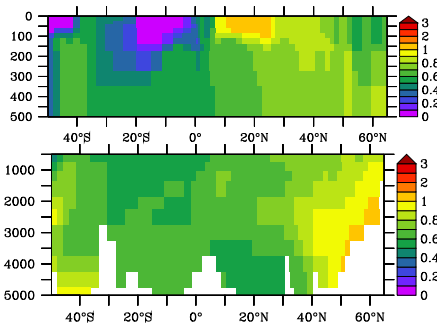
MEDUSA 1, GA-02



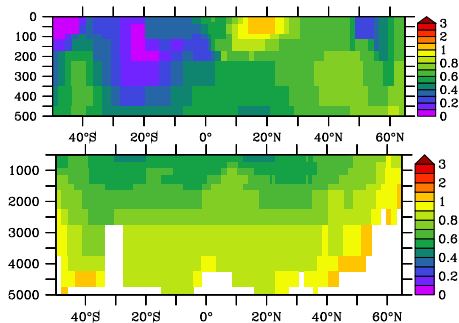
MEDUSA 2, GA-02



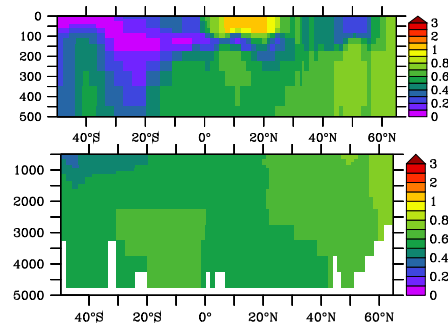
MITecco, GA-02



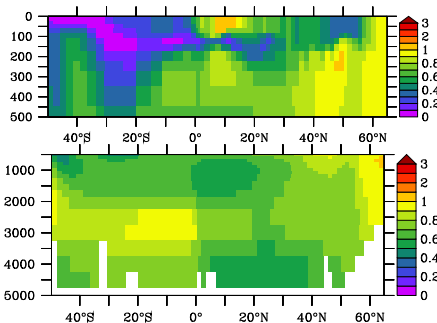
MITigsm, GA-02



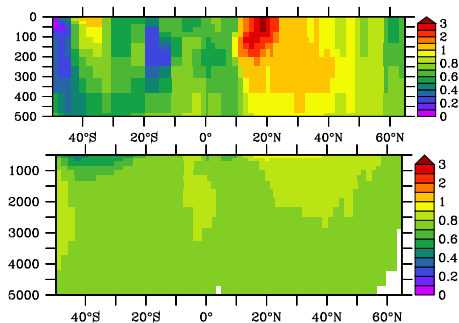
PISCES 1, GA-02



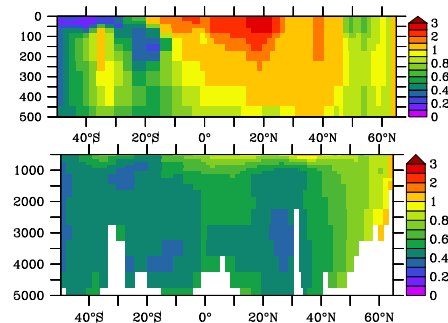
PISCES 2, GA-02



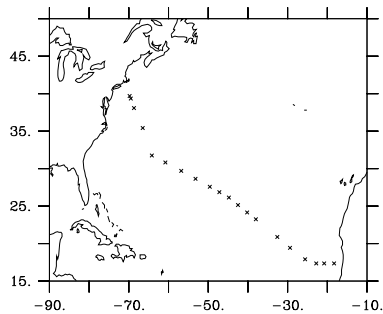
RECOM, GA-02



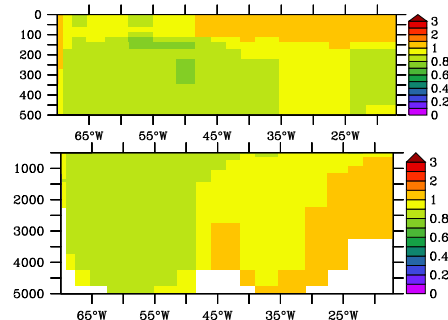
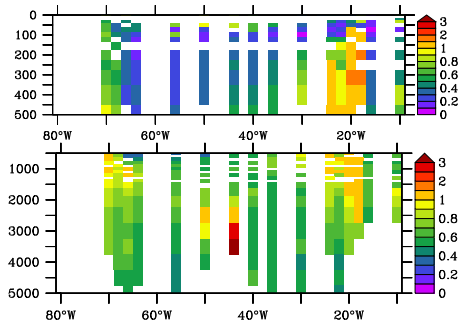
TOPAZ, GA-02



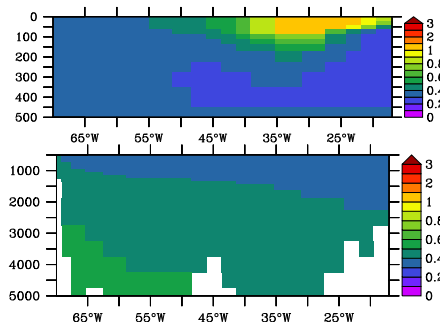
GA-03, Cruise



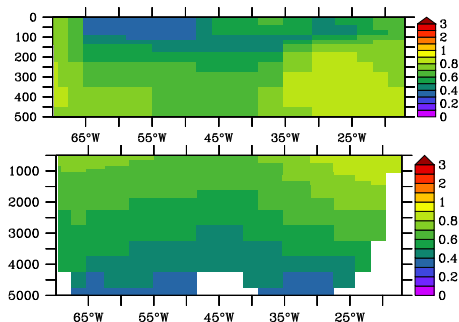
BEC, GA-03



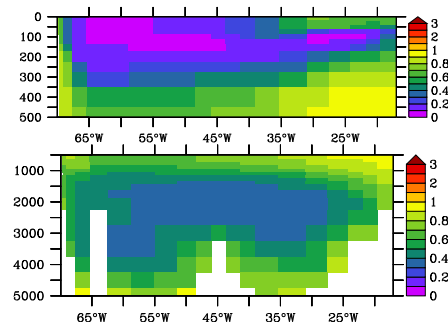
BFM, GA-03



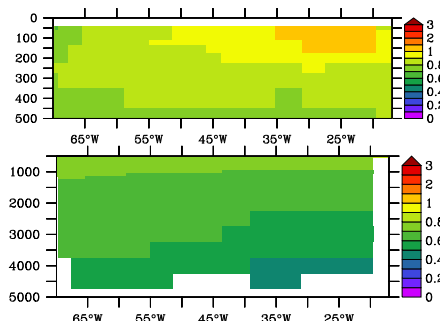
BLING, GA-03



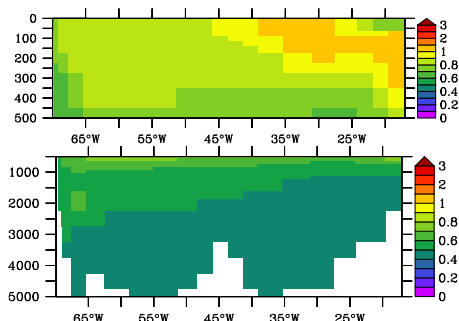
COBALT, GA-03



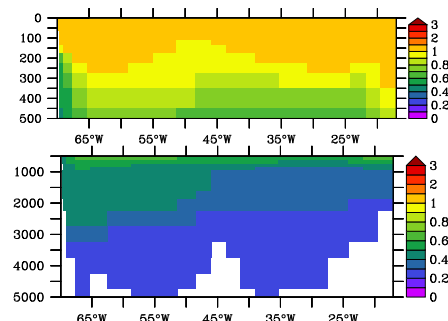
GENIE, GA-03



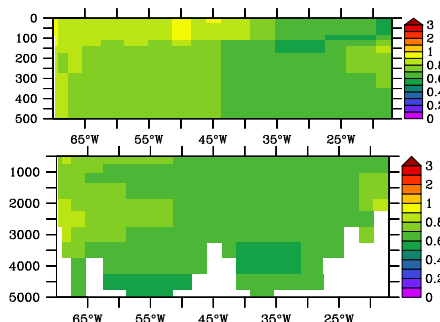
MEDUSA 1, GA-03



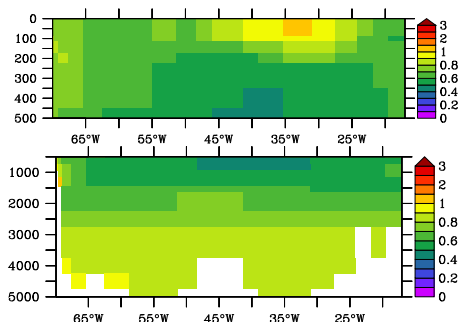
MEDUSA 2, GA-03



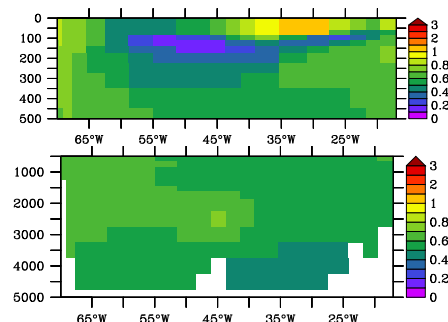
MITecco, GA-03



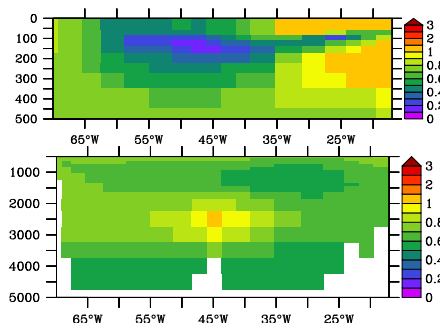
MITigsm, GA-03



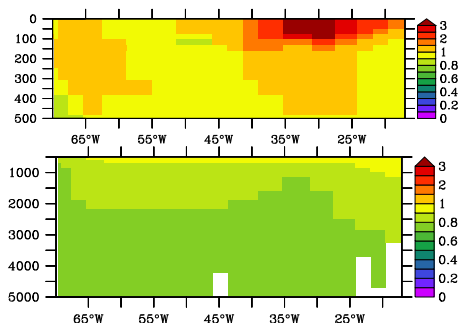
PISCES 1, GA-03



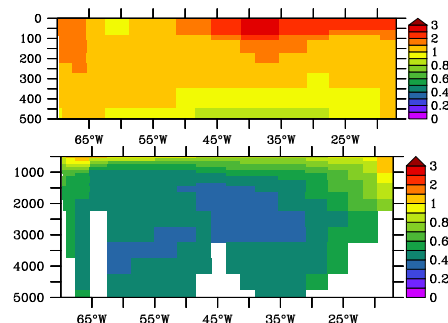
PISCES 2, GA-03



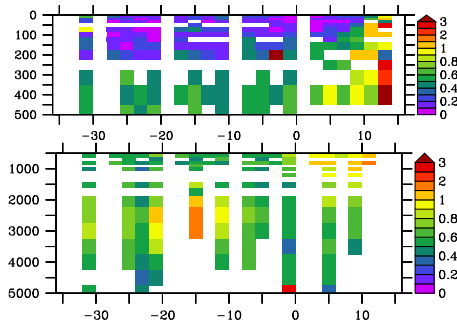
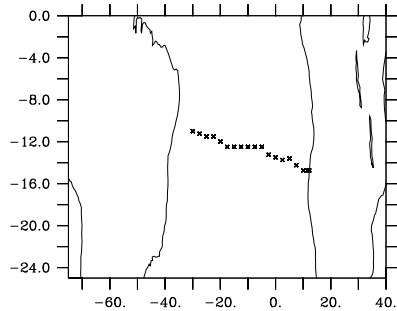
RECOM, GA-03



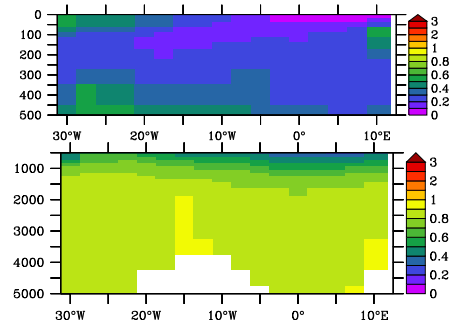
TOPAZ, GA-03



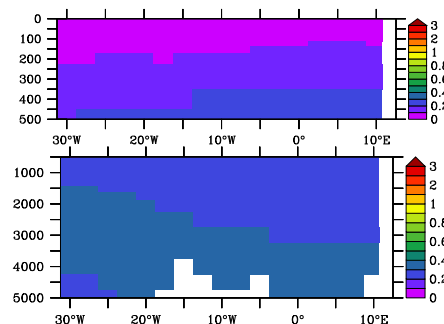
CoFeMUG, Cruise



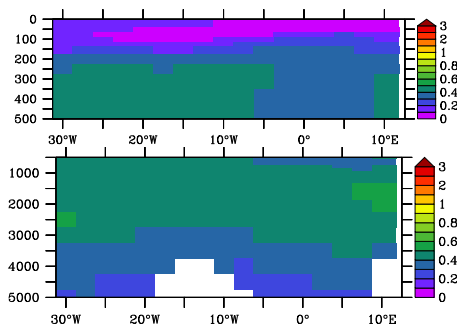
BEC, GA-03



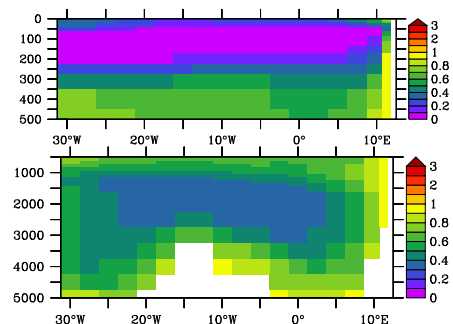
BFM, GA-03



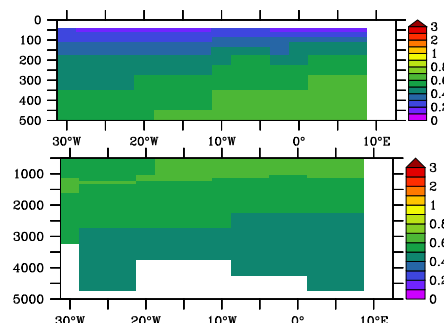
BLING, GA-03



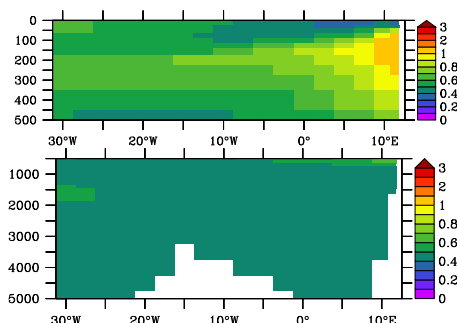
COBALT, GA-03



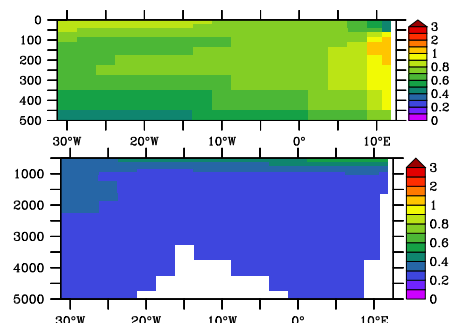
GENIE, GA-03



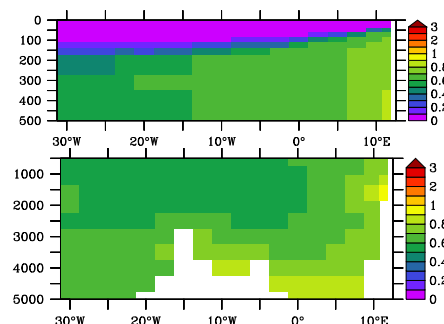
MEDUSA 1, GA-03



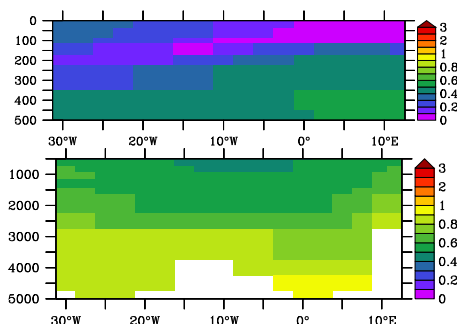
MEDUSA 2, GA-03



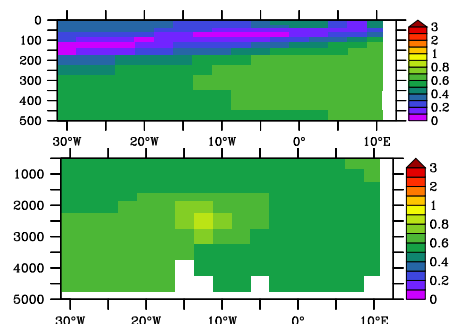
MITecco, GA-03



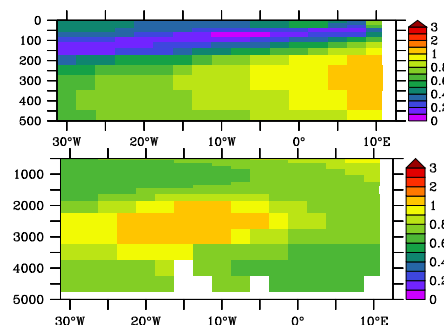
MITigsm, GA-03



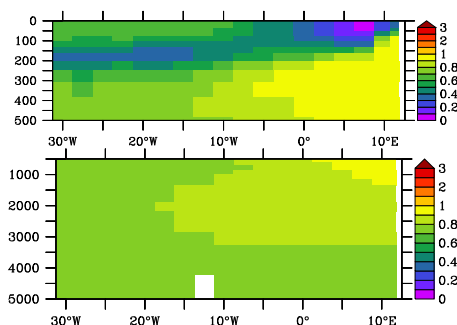
PISCES 1, GA-03



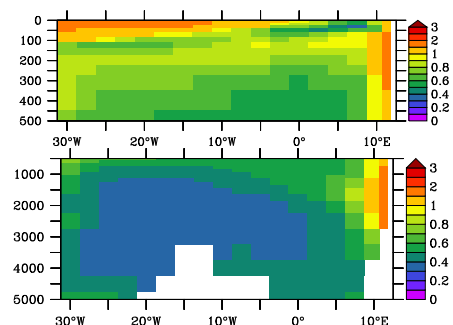
PISCES 2, GA-03



RECOM, GA-03

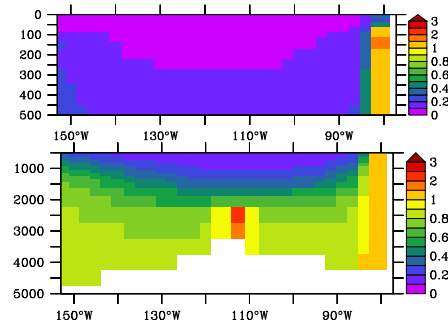
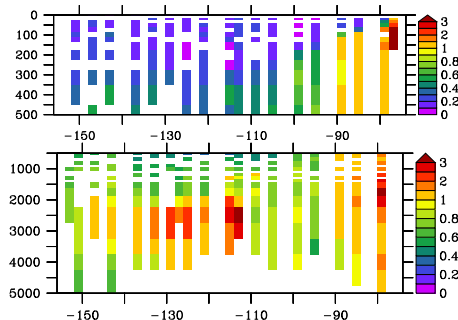
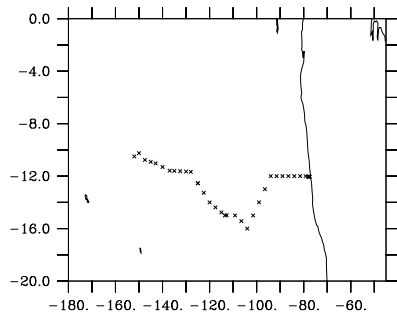


TOPAZ, GA-03



GP-16 Cruise

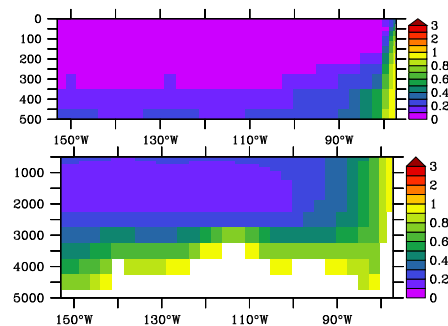
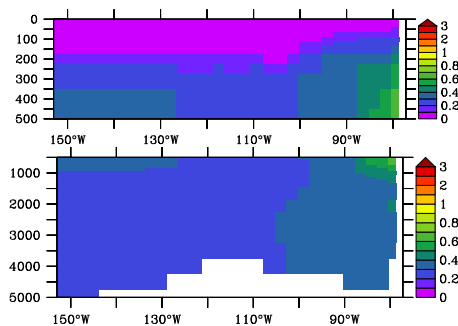
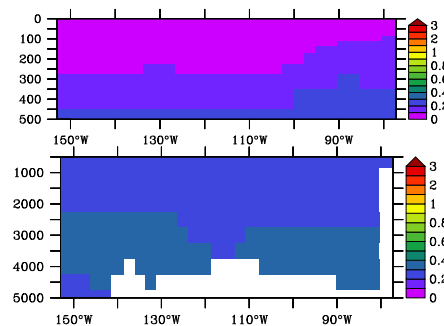
BEC, GP-16



BFM, GP-16

BLING, GP-16

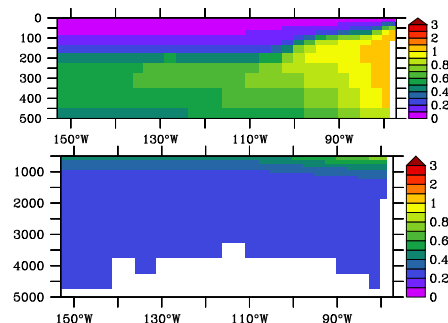
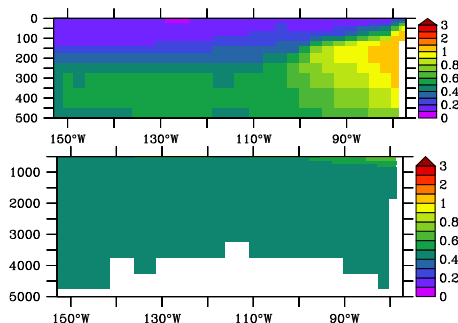
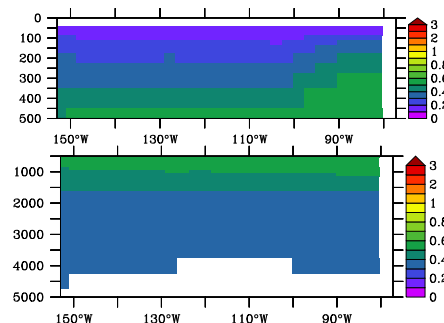
COBALT, GP-16



GENIE, GP-16

MEDUSA 1, GP-16

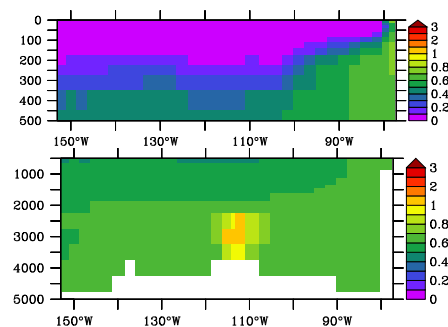
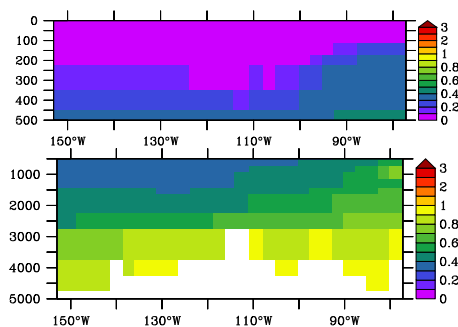
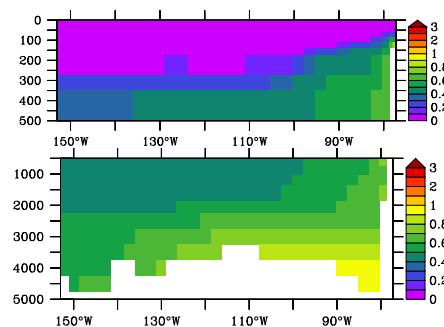
MEDUSA 2, GP-16



MITecco, GP-16

MITigsm, GP-16

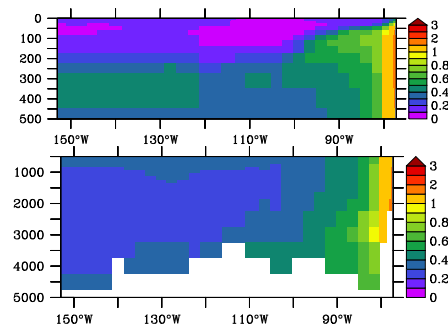
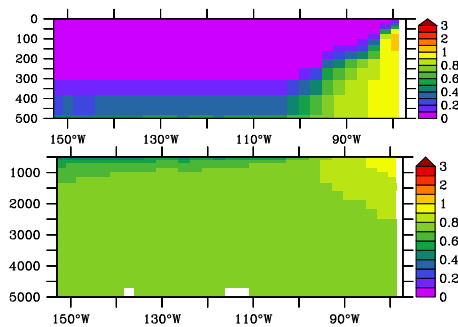
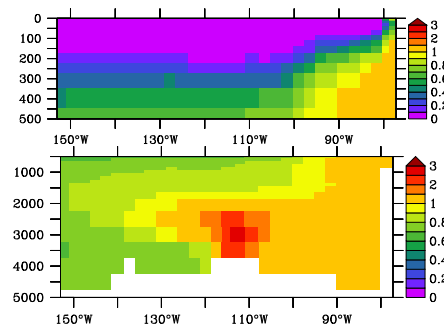
PISCES 1, GP-16



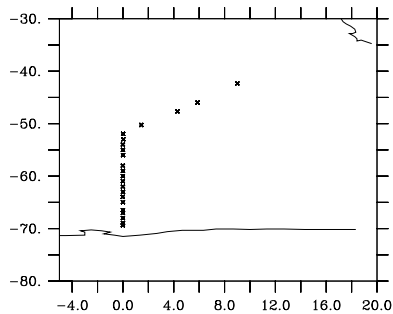
PISCES 2, GP-16

RECOM, GP-16

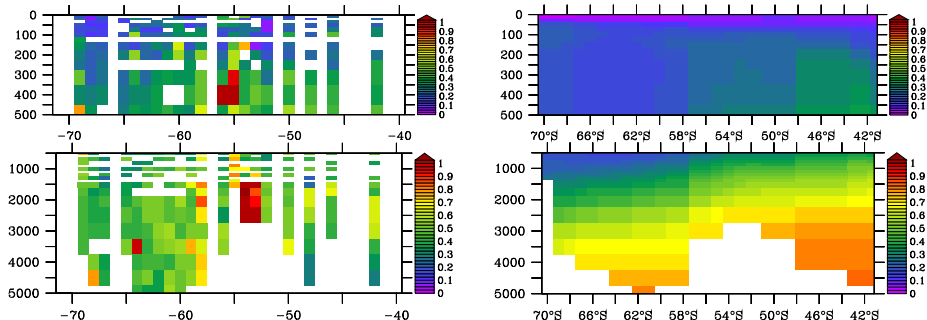
TOPAZ, GP-16



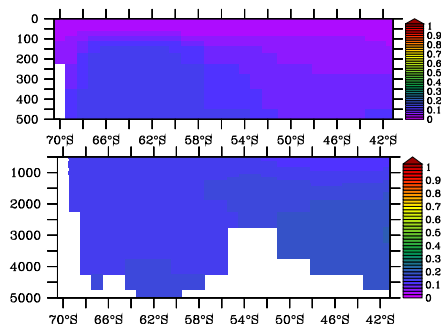
GIKY-5, Cruise



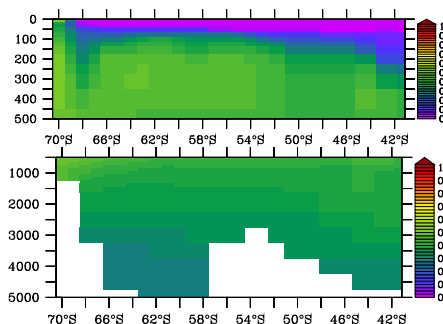
BEC, GIKY-5



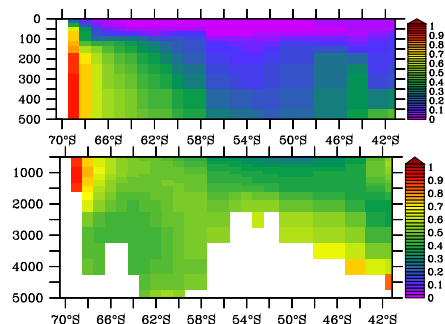
BFM, GIKY-5



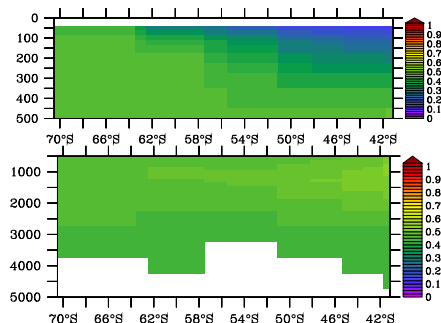
BLING, GIKY-5



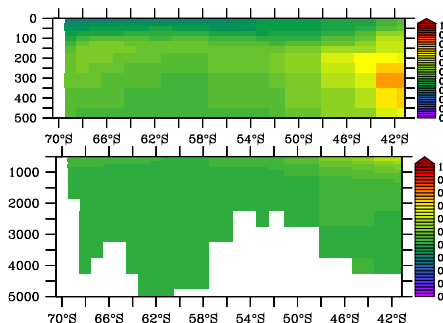
COBALT, GIKY-5



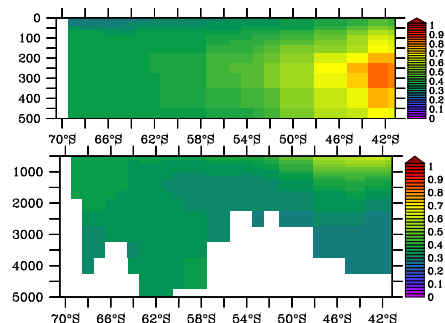
GENIE, GIKY-5



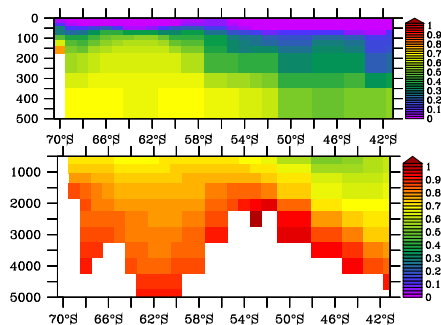
MEDUSA 1, GIKY-5



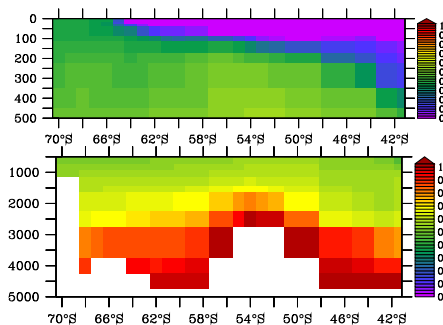
MEDUSA 2, GIKY-5



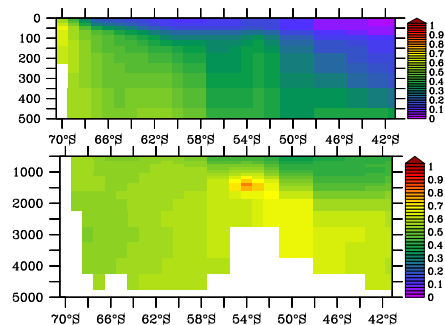
MITecco, GIKY-5



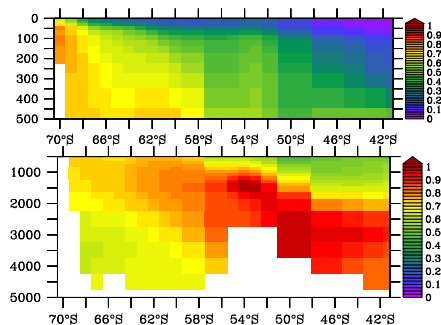
MITigsm, GIKY-5



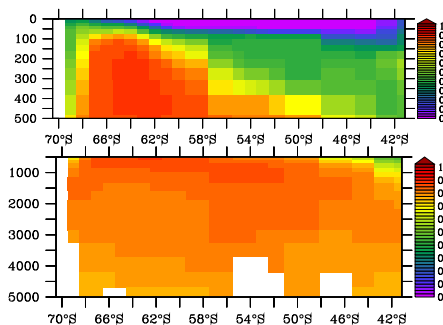
PISCES 1, GIKY-5



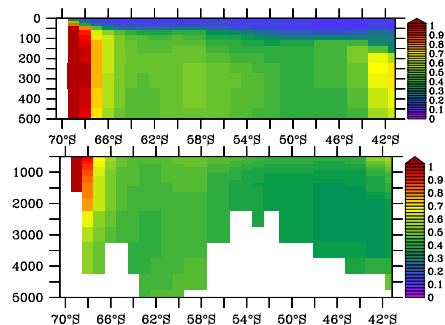
PISCES 2, GIKY-5



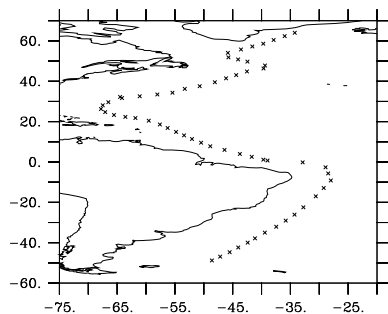
RECOM, GIKY-5



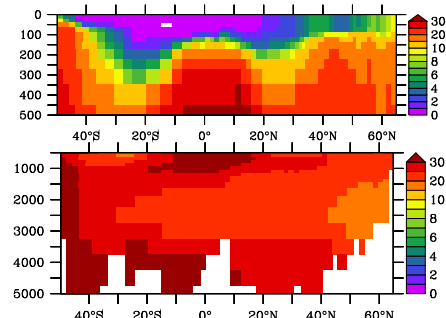
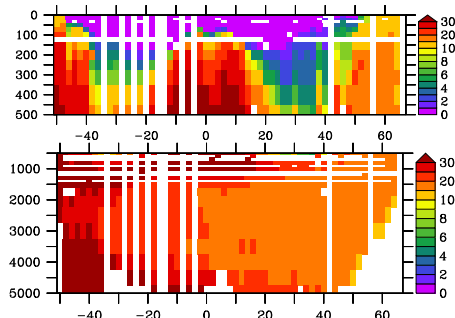
TOPAZ, GIKY-5



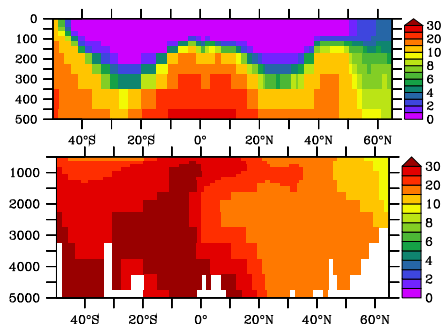
GA-02, Cruise



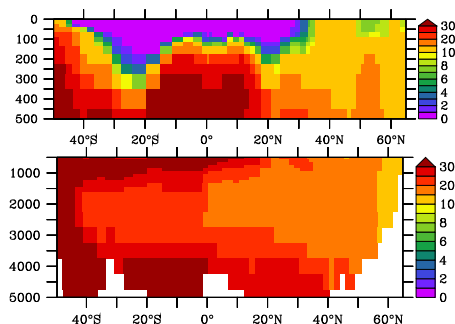
BEC, GA-02



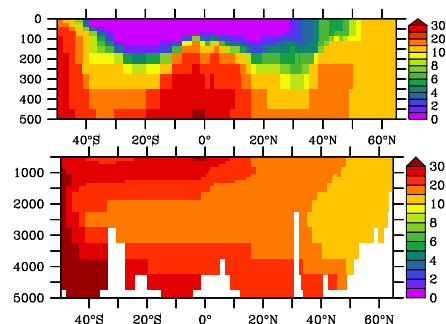
BFM, GA-02



BLING, GA-02

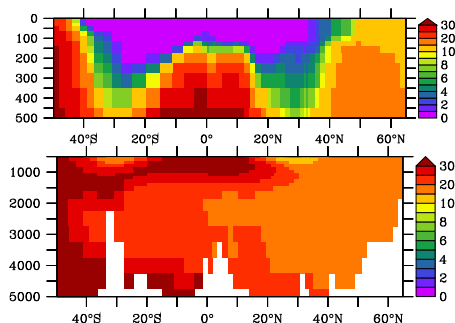


COBALT, GA-02

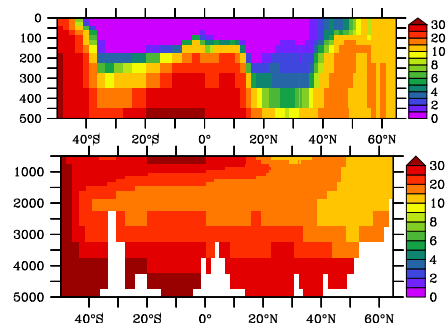


GENIE, GA-02

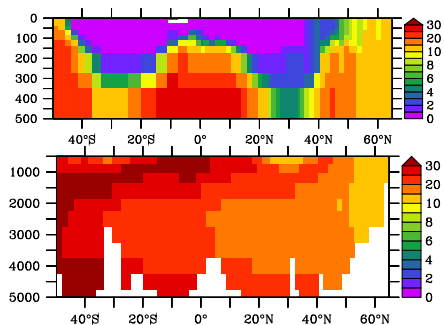
MEDUSA 1, GA-02



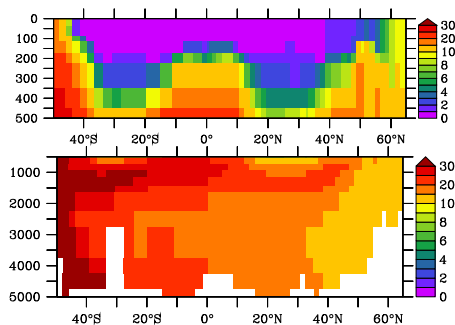
MEDUSA 2, GA-02



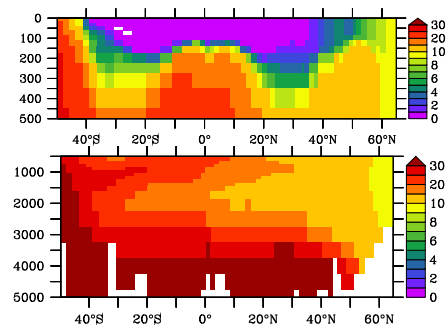
MITecco, GA-02



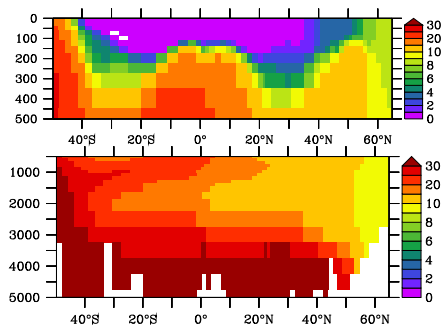
MITigsm, GA-02



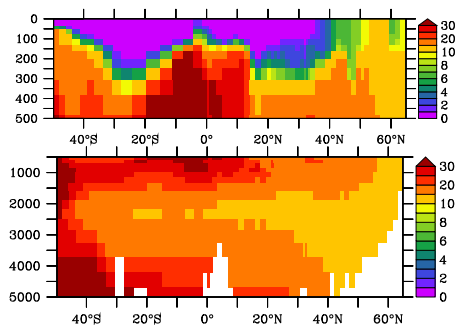
PISCES 1, GA-02



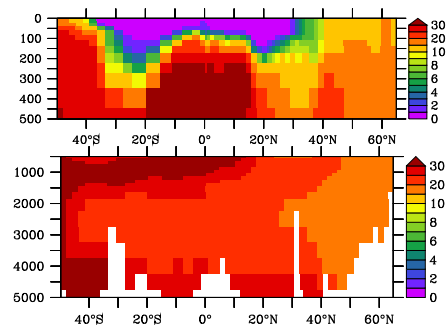
PISCES 2, GA-02



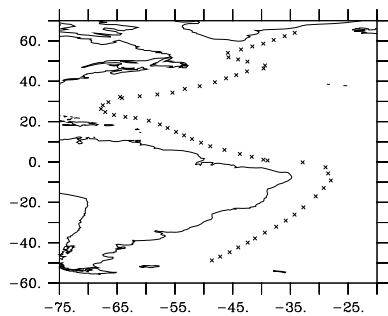
RECOM, GA-02



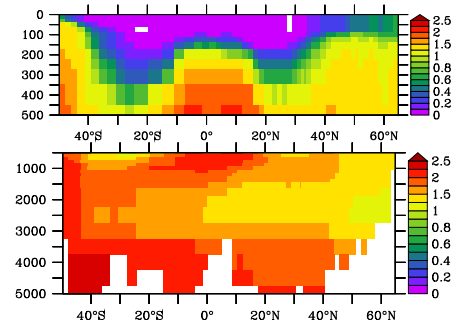
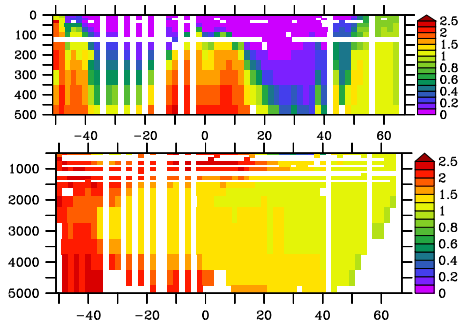
TOPAZ, GA-02



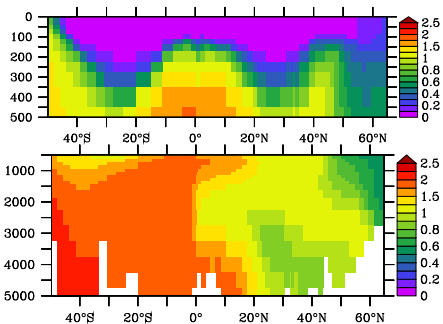
GA-02, Cruise



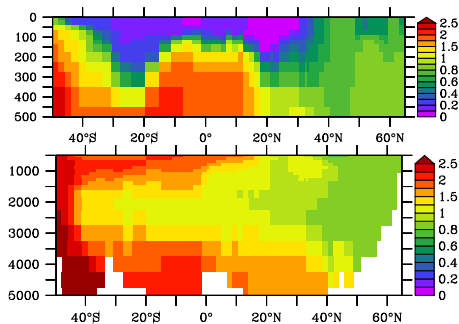
BEC, GA-02



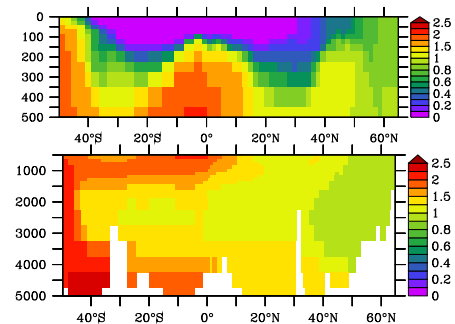
BFM, GA-02



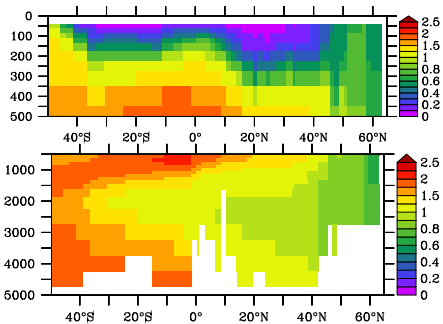
BLING, GA-02



COBALT, GA-02



GENIE, GA-02



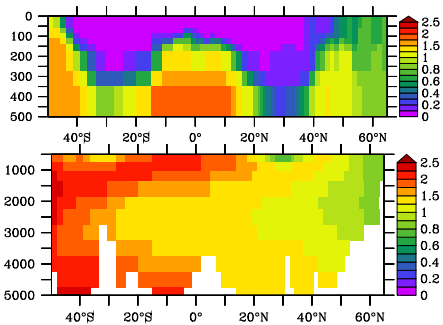
MEDUSA 1, GA-02



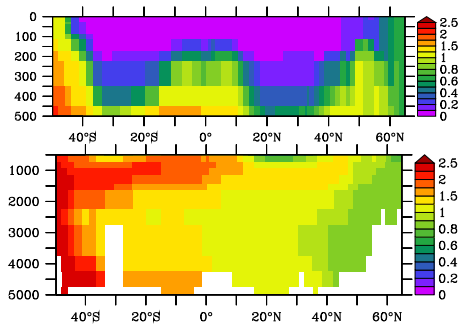
MEDUSA 2, GA-02



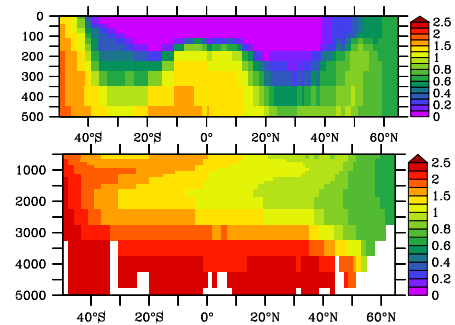
MITecco, GA-02



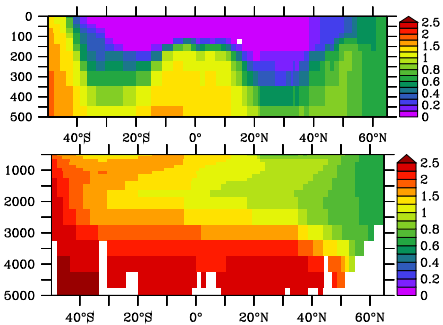
MITigsm, GA-02



PISCES 1, GA-02



PISCES 2, GA-02



RECOM, GA-02

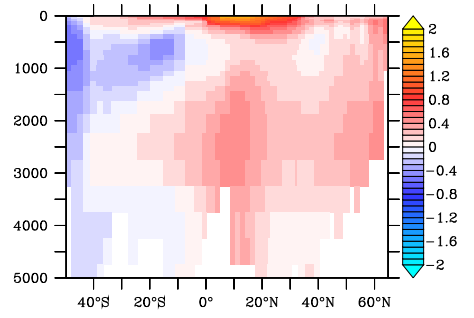
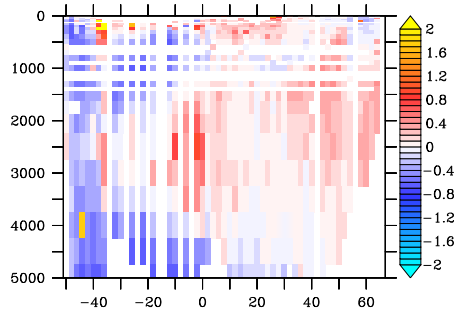
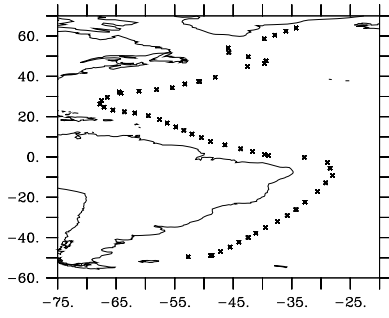


TOPAZ, GA-02



Festar based on Nitrate, GA-02, Cruise

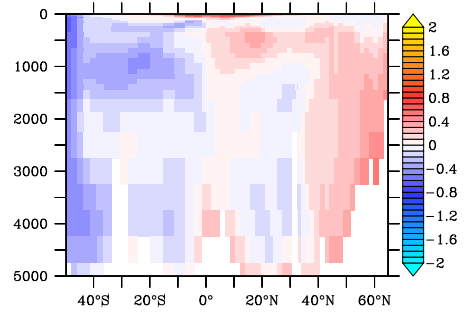
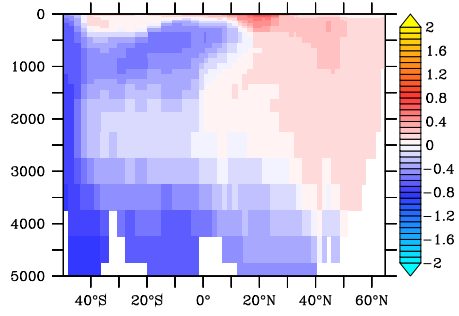
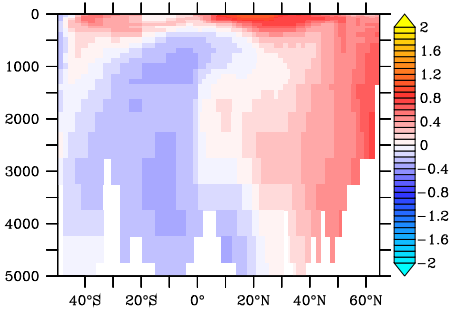
BEC



BFM

BLING

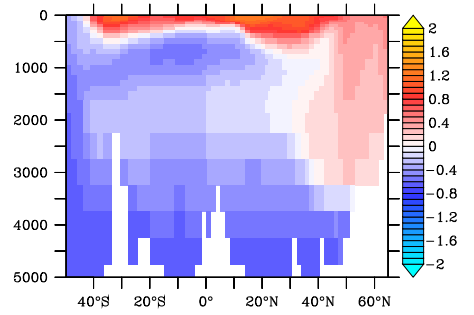
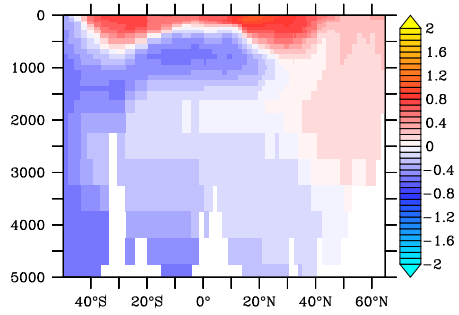
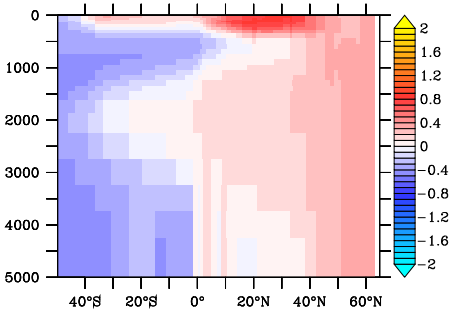
COBALT



GENIE

MEDUSA1

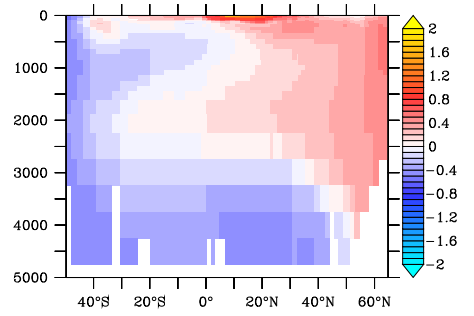
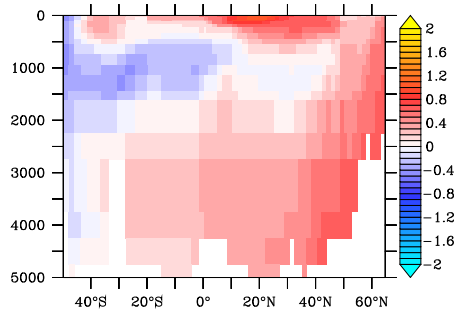
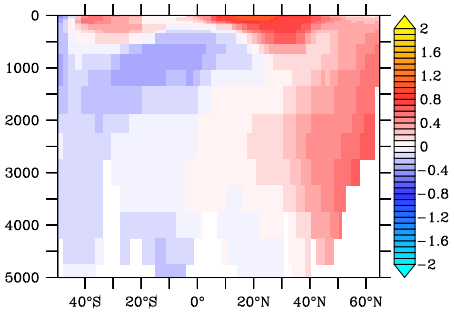
MEDUSA2



MITecco

MITigsm

PISCES1



PISCES2

RECOM

TOPAZ

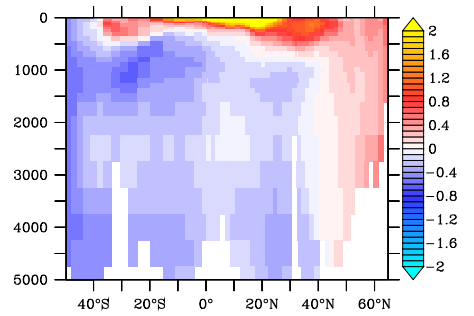
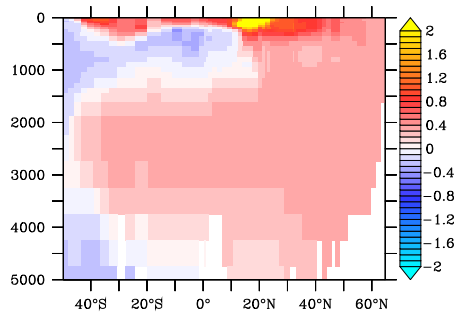
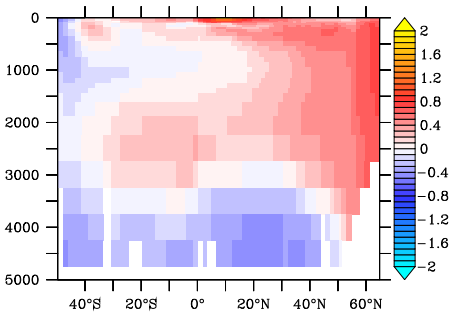


Table 1 A summary of the FeMIP models. Indicated is the number of years of model spin up, which iron sources are represented, whether ligands are present, fixed, or dynamic, whether Fe chemistry is considered implicitly (i.e. a threshold) or explicitly (i.e. computing free Fe as a function of ligands and conditional stability of complexes), the order of Fe scavenging (1 = uniform rate, 2 = also a function of particles), whether colloidal pumping loss of DFe is represented, if biological have a fixed or variable demand for Fe (Fe quota), if recycling is a fixed rate of variable (as a function of their Fe demand), how many particulate Fe pools are represented (if any) and whether the regeneration efficiency of particulate Fe is specific or is coupled to other tracers (carbon or nitrogen for example).

Model	Spin Up	Fe sources				Fe chemistry				Fe biology		Particles	
		Dust	Sed.	Hydro.	River	Ligands	Speciation	Scav	Colloids	Demand	Recycling	Pools	Regen.
<i>BEC</i>	290 yrs	yes	yes	yes	yes	Fixed	Implicit	2	no	Variable	Fixed	0	Coupled
<i>BFM</i>	30 yrs	yes	no	no	yes	Fixed	Explicit	1	no	Variable	Variable	1	Coupled
<i>BLING</i>	1,800 yrs	yes	yes	no	no	Fixed	Explicit	2	no	Variable	Fixed	1	Coupled
<i>COBALT</i>	100 yrs	yes	yes	no	no	Fixed	Explicit	1	no	Variable	Variable	1	Specific
<i>GENIE</i>	10,000 yrs	yes	no	no	no	Fixed	Explicit	2	no	Variable	Variable	1	Coupled
<i>MEDUSA1</i>	40 yrs	yes	no	no	no	Fixed	Explicit	1	no	Fixed	Fixed	1	Coupled
<i>MEDUSA2</i>	140 yrs	yes	yes	no	no	Fixed	Explicit	1	no	Fixed	Fixed	1	Coupled
<i>MITecco</i>	40 yrs	yes	yes	no	no	Fixed	Explicit	2	no	Fixed	Variable	1	Coupled
<i>MITigsm</i>	190 yrs	yes	yes	no	no	Fixed	Explicit	2	no	Fixed	Variable	1	Coupled
<i>PISCES1</i>	3,000 yrs	yes	yes	yes	yes	Fixed	Explicit	2	yes	Variable	Variable	2	Coupled
<i>PISCES2</i>	3,000 yrs	yes	yes	yes	yes	Dynamic	Explicit	2	yes	Variable	Variable	2	Coupled
<i>REcoM</i>	1,000 yrs	yes	yes	no	no	Fixed	Explicit	2	no	Both	Fixed	1	Coupled
<i>TOPAZ</i>	1,000 yrs	yes	yes	no	no	Dynamic	Explicit	2	no	Variable	Variable	1	Coupled

Table 2. A summary of the magnitude of the Fe sources, the total and average Fe inventories, and the residence time of Fe across the FeMIP models.

Model	Fe sources Gmol yr⁻¹				Total	Fe inventory x10¹¹ mol	Average Fe (nmoles L⁻¹)	Residence Time (yrs)
	Dust	Sed	Hydro	Rivers				
<i>BEC</i>	21.9	84.6	17.7	0.34	124.5	10.1	0.74	8.1
<i>BFM</i>	1.4	0	0	0.06	1.4	8.8	0.65	626.3
<i>BLING</i>	3.3	9.1	0	0	12.4	5.3	0.37	42.4
<i>COBALT</i>	32.5	155	0	0	182.5	6.8	0.50	3.7
<i>GENIE</i>	1.8	0	0	0	1.8	10.1	0.48	560.0
<i>MEDUSA1</i>	2.7	0	0	0	2.7	6.3	0.46	232.0
<i>MEDUSA2</i>	3.4	2.9	0	0	6.8	4.8	0.35	69.9
<i>MITecco</i>	3.5	104	0	0	107.5	8.8	0.65	8.2
<i>MITigsm</i>	1.4	194	0	0	195.4	9.0	0.66	4.6
<i>PISCES1</i>	32.7	26.6	11.3	2.5	71.0	8.1	0.59	11.5
<i>PISCES2</i>	32.7	26.6	11.3	2.5	71.0	11.2	0.81	15.7
<i>REcoM</i>	3.7	0.6	0	0	4.3	12.5	0.73	291.6
<i>TOPAZ</i>	13.8	74.8	0	0	88.6	6.8	0.50	7.6
				Mean	66.9	8.3	0.58	144.7
				St dev	67.1	2.2	0.14	175.8

Table 3. Correlation coefficient (R) and in parentheses the mean bias (nM) between the different FeMIP models and the expanded database of Tagliabue et al. [2012] across different depth bins. Average dissolved iron data (nM) for the different depth strata is presented in the final row. The iron data are gridded on the FeMIP grid as described in the text.

	ALL	0-100	100-500	500-1000	2000-5000
Model					
<i>BEC</i>	0.51 (-0.02)	0.48 (0.23)	0.52 (-0.05)	0.47 (-0.15)	0.31 (0.01)
<i>BFM</i>	0.39 (-0.48)	0.34 (-0.29)	0.36 (-0.47)	0.33 (-0.52)	-0.03 (-0.48)
<i>BLING</i>	0.37 (-0.33)	0.37 (-0.13)	0.49 (-0.17)	0.46 (-0.26)	0.01 (-0.44)
<i>COBALT</i>	0.45 (-0.25)	0.38 (-0.19)	0.48 (-0.25)	0.51 (-0.19)	-0.11 (-0.25)
<i>GENIE</i>	0.25 (-0.28)	0.43 (-0.02)	0.46 (-0.11)	0.43 (-0.20)	-0.14 (-0.40)
<i>MEDUSA1</i>	-0.01 (-0.24)	0.37 (0.23)	0.38 (0.04)	0.07 (-0.24)	0.07 (-0.37)
<i>MEDUSA2</i>	-0.14 (-0.32)	0.35 (0.29)	0.37 (0.07)	-0.06 (-0.30)	-0.10 (-0.51)
<i>MITecco</i>	0.39 (-0.12)	0.34 (-0.10)	0.36 (-0.09)	0.33 (-0.14)	-0.03 (-0.11)
<i>MITigsm</i>	0.37 (-0.14)	0.04 (-0.22)	0.42 (-0.24)	0.29 (0-.24)	-0.13 (-0.04)
<i>PISCES1</i>	0.47 (-0.23)	0.36 (-0.06)	0.47 (-0.17)	0.47 (-0.03)	0.21 (-0.27)
<i>PISCES2</i>	0.51 (-0.04)	0.37 (0.03)	0.52 (0.01)	0.43 (-0.03)	0.35 (-0.05)
<i>REcoM</i>	0.39 (-0.05)	0.33 (0.25)	0.40 (0.01)	0.44 (-0.01)	-0.04 (-0.12)
<i>TOPAZ</i>	0.10 (-0.13)	0.42 (0.67)	0.27 (0.26)	0.33 (-0.12)	0.01 (-0.34)
Data	0.64	0.52	0.63	0.76	0.90